Stability of buoyant convection in a layer submitted to acoustic streaming

W. Dridi, D. Henry,* and H. Ben Hadid
Laboratoire de Mécanique des Fluides et d'Acoustique, CNRS/Université de Lyon–École Centrale de Lyon/Université Lyon 1/INSA de Lyon–ECL, 36 Avenue Guy de Collongue, 69134 Ecully Cedex, France
(Received 24 November 2009; published 11 May 2010)

The linear stability of the flows induced in a fluid layer by buoyant convection (due to an applied horizontal temperature gradient) and by acoustic streaming (due to an applied horizontal ultrasound beam) is studied. The vertical profiles of the basic flows are determined analytically, and the eigenvalue problem resulting from the temporal stability analysis is solved by a spectral Tau Chebyshev method. Pure acoustic streaming flows are found to be sensitive to a shear instability developing in the plane of the flow (two-dimensional instability), and the thresholds for this oscillatory instability depend on the normalized width H_b of the ultrasound beam with a minimum for $H_b=0.32$. Acoustic streaming also affects the stability of the buoyant convection. For a centered beam, effects of stabilization are obtained at small Prandtl number Pr for large beam widths H_b (two-dimensional shear instability) and for moderate Pr (three-dimensional oscillatory instability), but destabilization is also effective at small Pr for small beam widths H_b and at large Pr with a spectacular decrease of the thresholds of the three-dimensional steady instability. An adequate decentring of the ultrasound beam can enhance the stabilization. Insight into the stabilizing and destabilizing mechanisms is gained from the analysis of the fluctuating energy budget associated with the disturbances at threshold. The modifications affecting the two-dimensional shear instability thresholds are strongly connected to modifications of the velocity fluctuations when acoustic streaming is applied. Concerning the three-dimensional steady instability, the spectacular decrease of the thresholds is explained by the extension of the zone with inverse stratification in the lower half of the layer.

DOI: 10.1103/PhysRevE.81.056309 PACS number(s): 47.20.Bp, 47.20.Ft, 47.11.Kb

I. INTRODUCTION

Directional solidification is used in the processing of semiconducting and optoelectronic materials, whose performance relies on the homogeneity of the crystalline material [1]. In the horizontal Bridgman technique, the molten crystal is contained in a crucible which is withdrawn horizontally from a furnace. Thus, the melt is subject to a horizontal temperature gradient, which drives endwall convection. In practice, the flow which is first unicellular evolves with the increase of the temperature gradient, undergoes bifurcations and becomes unsteady, and eventually turbulence sets in for large temperature differences. It is now well known that instabilities in the melt phase adversely affect the quality of the crystal, as they impose temperature fluctuations at the solidification front and lead to striations in the crystalline product [2]. The control of the flows and of the instabilities in the melt phase has then become an important research objective for the past decade. Microgravity and more commonly magnetic fields have been used for crystal growth applications as they allow the damping of the convective flow in the melt. They are, however, costly and heavy technologies. An alternative could be the use of ultrasound waves which can reorganize the flow in the melt through the generation of acoustic streaming. It is this possibility we want to study in this paper.

Acoustic streaming describes a steady flow generated by an ultrasound wave propagating in a fluid. This effect was first observed in 1831 by Faraday [3]. It is now well known that it is a nonlinear effect which owes its origin to the action of Reynolds stresses (mean momentum flux due to the ultrasound wave) and the dissipation of acoustic energy flux. More precisely, it is the dissipation (or spatial attenuation) of acoustic energy flux that permits gradients in momentum flux to force acoustic streaming motions [4,5]. There are two main types of acoustic streaming: Eckart streaming in which the dissipation takes place in the main body of the fluid [6], and Rayleigh streaming in which the dissipation is associated with boundary layers at solid surfaces [7]. In our study we will consider Eckart streaming in which the flow, generated inside the ultrasound beam, moves the fluid away from the ultrasound source. Such streaming motions have been used to move fluids in microfluidic devices [8,9], induce chaotic mixing [10], and even improve the quality of crystals obtained by directional solidification processes [11].

The main studies concerning the action of acoustic streaming on directional solidification processes have been performed experimentally by Kozhemyakin and his coworkers. The first studies [11–13] have shown that acoustic streaming was able to decrease or even eliminate the striations in different single crystals grown by the Czochralski process. Kozhemyakin [14] then studied the influence of ultrasound waves on the convective flows thermally induced in distilled water. The advantage of distilled water is that it is transparent and allows easy flow measurements by optical methods, but also that some of its properties, such as sound velocity and acoustic spatial attenuation factor, are similar to that of liquid metals as InSb melts [15]. The experiment models a Czochralski configuration used for the growth of $Ga_xIn_{1-x}Sb$ single crystals. It is shown that the ultrasound waves at high frequency allow to reduce the convection. A strong reduction of the flow oscillations is also observed which is shown to be connected to the acoustic standing

*daniel.henry@ec-lyon.fr

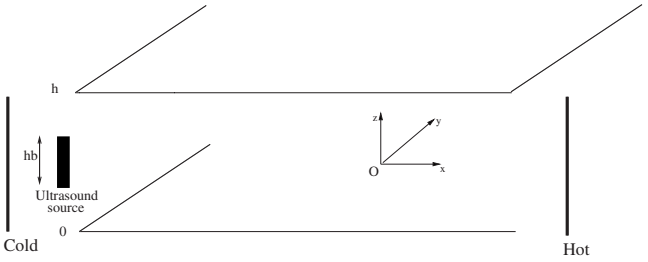

FIG. 1. Schematic diagram of the laterally heated layer subject to an ultrasound beam.

waves appearing between the quartz waveguide and the model solid/liquid interface. More recently, Kozhemyakin *et al.* [16] investigated the influence of ultrasound on the growth striations and electrophysical properties of $Ga_xIn_{1-x}Sb$ single crystals. They show that the use of ultrasound allows to reduce the striations in the single crystals, which induces an improvement of the crystal properties, e.g., an increase of the carrier mobility and the thermal emf, and a decrease of the resistivity.

Our numerical work on the subject has considered a different crystal growth configuration, namely, the horizontal Bridgman configuration. More precisely, the numerical studies have investigated the influence of acoustic streaming on the convective flows induced by a horizontal temperature gradient, which are typical of the flows in horizontal Bridgman crystal growth configurations. A first study was focused on the stabilizing influence of the Rayleigh streaming on convection induced in a three-dimensional cavity [17]. The other studies were concerned by Eckart streaming. The action of the Eckart streaming on the convection instabilities was first studied in side-heated cavities with thermally insulated boundaries, three-dimensional cavities of different lengths [15], or an infinite layer [18]. Preliminary results have also been obtained in the case of an infinite layer with thermally conducting boundaries [19,20]. These studies have shown that Eckart streaming can have a stabilizing effect on the convective flows, but only in some parameter ranges.

The objective of this work is to precise and extend the results in the case of the infinite layer with thermally conducting boundaries and to deepen our understanding of the influence of Eckart streaming on these convective flows typical of horizontal Bridgman crystal growth configurations. We will determine the flows induced in such a side-heated fluid layer submitted to an ultrasound beam and study their stability with respect to the dominant instability modes. We will focus our study on the influence of acoustic streaming on these instabilities, and for that will largely vary the characteristic parameters, i.e., the beam width and position, and the intensity of the force created by the ultrasound wave. We will finally analyze the stabilizing or destabilizing effects induced by acoustic streaming through energy analyses.

II. GOVERNING EQUATIONS AND BASIC FLOW

We consider an incompressible liquid layer of thickness h (in the vertical z direction) confined between two infinite horizontal walls (Fig. 1). This layer is subject to a horizontal temperature gradient $\nabla\tilde{T}$ along the longitudinal x direction and to a radiation pressure caused by an ultrasound beam generated in the x direction by a transducer. The fluid is assumed to be Newtonian with constant kinematic viscosity ν and thermal diffusivity κ. According to the Boussinesq approximation, density variations are restricted to the buoyancy term and taken as a linear variation of the temperature, $\rho=\rho_0(1-\beta(\tilde{T}-\tilde{T}_0))$, where β is the thermal expansion coefficient and $\tilde{T}_0$ is a reference temperature. The ultrasound beam, which is applied inside the layer, has a characteristic width h_b ($h_b<h$) in the vertical z direction and is uniform in the transverse y direction. The divergence of the beam is thus assumed to be small, which has been shown to be a reasonable hypothesis in melt configurations [15]. The ultrasound field is also assumed to be a plane wave of frequency f traveling in the positive x direction. Since Lighthill [4], it is well known that the attenuation of an ultrasound wave in a viscous fluid gives rise to a body force acting within the ultrasound beam and equal to the spatial variation of the Reynolds stress. For a plane wave traveling in the positive x direction, following Nyborg [5] and Frampton *et al.* [9], it can be shown that the body force is oriented along the x axis and that its intensity is given by $F=\rho\alpha V_a^2 e^{-2\alpha x}$, where α is the amplitude attenuation coefficient for ultrasound, and V_a is the amplitude of the acoustic velocity oscillation [15]. Now, provided the attenuation of the wave is sufficiently weak (estimations in [15] give a few percents), a body force, which is constant ($F=\rho\alpha V_a^2$) inside the beam (over a height h_b) and zero above and below the beam, can be defined [6,8,15,19]. Following Lighthill [4], this body force can be introduced in the Navier-Stokes equations which, in our case, are coupled with an energy equation through the buoyancy term. If we consider h, h^2/ν, ν/h, $\rho_0\nu^2/h^2$, and $\nabla\tilde{T}h$ as scales for length, time, velocity, pressure, and temperature, respectively, the relevant dimensionless equations are

$$\boldsymbol{\nabla}\cdot\boldsymbol{V}=0, \tag{1}$$

$$\frac{\partial \boldsymbol{V}}{\partial t}+(\boldsymbol{V}\cdot\boldsymbol{\nabla})\boldsymbol{V}=-\boldsymbol{\nabla}P+\boldsymbol{\nabla}^2\boldsymbol{V}+\mathrm{Gr}\,T\boldsymbol{e}_z+A\,\delta_b\boldsymbol{e}_x, \tag{2}$$

$$\frac{\partial T}{\partial t}+(\boldsymbol{V}\cdot\boldsymbol{\nabla}T)=\frac{1}{\mathrm{Pr}}\boldsymbol{\nabla}^2T, \tag{3}$$

where the dimensionless variables are the velocity vector [$\boldsymbol{V}=(U,V,W)$], the pressure P, and the temperature T. In these equations, Gr is the Grashof number ($\mathrm{Gr}=g\beta\nabla\tilde{T}h^4/\nu^2$), Pr is the Prandtl number ($\mathrm{Pr}=\nu/\kappa$), and A is an acoustic streaming parameter defined as $A=\alpha V_a^2h^3/\nu^2$ [15]. (Note that the parameter A does not directly depend on the sound wave frequency f. This dependence is nevertheless effective through the acoustic attenuation coefficient α which is known to vary as f^2.) δ_b is a function of z which is 1 inside the acoustic beam and 0 outside. The boundary conditions at the horizontal walls (located at $z=-1/2$ and $z=1/2$) are no slip conditions, and perfectly conducting thermal conditions.

Note that we have not introduced the Rayleigh streaming influence in our model, despite the fact that the ultrasound

beam could be close to the boundaries. In fact, according to Frampton *et al.* [9], the boundary layer induced streaming is a very small contributor to the total streaming in large-scale channels (typically with a size of at least 1 mm). More precisely, for a plane traveling wave occupying the whole height of a channel, it was shown by Nyborg [5] that the ratio of the maximum of the "Rayleigh force" to the "Eckart force" is equal to $0.23k/\alpha$ (where $k=2\pi f/c$ is the wave number and c is the sound velocity), and in water at 20° for a frequency of 1 MHz, the ratio k/α is 1.66×10^5, indicating a much stronger intensity of the Rayleigh force. The "Rayleigh force" however occurs over a very small portion of the channel height (less than 1 μm along the boundaries), whereas the "Eckart force" is approximately constant and occurs on the whole height of the channel. The relative ability of these forces to generate streaming flows has to be estimated. As an example, for a plane traveling wave in a channel with open ends, Nyborg [5] showed that the average Rayleigh streaming velocity is about $V_R=V_a^2/4c$, whereas the average Eckart streaming velocity (parabolic pattern) is $V_E=\alpha V_a^2h^2/12\nu$. In water at 20° for a channel height h of 5 cm and a frequency of 1 MHz, the ratio V_R/V_E is about 2.9×10^{-5}. The results for liquid metals are not very different. The ratio k/α is really similar to that for water (due to similar values of the dynamic viscosity μ and attenuation coefficient α). The ratio V_R/V_E can be estimated for gallium with a kinematic viscosity $\nu=2.87\times10^{-7}$ m^2/s at 346 K [21] in a channel with a typical height of a few centimeters ($h=5$ cm, for instance) and an acoustic frequency of 1 MHz. In such conditions the ratio V_R/V_E is still very small, about 9.2×10^{-6}. It is thus shown that the streaming flow induced by a traveling wave in not too narrow cavities (as those used for crystal growth applications) is predominantly generated by Eckart streaming, the Rayleigh streaming contribution being really negligible. As pointed out by Frampton *et al.* [9], this is not true in microfluidic devices.

We now consider the layer as infinitely long in both horizontal x and y directions, but we also assume that there exist two vertical boundaries (oriented perpendicular to the x direction and located at $x=\pm\infty$) which will allow the flow to return (inducing a zero flow rate in each section of the layer at fixed x) without reflecting the ultrasound beam. In that case, a stationnary parallel flow solution depending only on the vertical z coordinate can be obtained [19]. This solution is governed by the following equations:

$$\frac{\partial^2 U_0}{\partial z^2}-\frac{\partial P_0}{\partial x}+A\,\delta_b=0, \tag{4}$$

$$-\frac{\partial P_0}{\partial z}+\mathrm{Gr}\,T_0=0, \tag{5}$$

$$\frac{\partial^2 T_0}{\partial z^2}=\mathrm{Pr}\,U_0, \tag{6}$$

with $U_0=U_0(z)$, $T_0=T_0(x,z)=x+T_i(z)$, and $\int_z U_0 dz=0$.

In the case of pure acoustic streaming effect, Gr=0, and from Eq. (5), P_0 is only a function of x. Then, from Eq. (4), $\partial P_0/\partial x$ is equal to terms only depending on z and must then be a constant C. Equation (4) will then give

$$\frac{\partial^2 U_{ac}}{\partial z^2}-C+A\,\delta_b=0. \tag{7}$$

The solution, quadratic in z inside and outside the beam, can be obtained easily assuming no slip conditions at the walls ($U_{ac}=0$), continuity conditions for U_{ac} and $\partial U_{ac}/\partial z$ at the beam boundary, and mass conservation. In the case where the beam is centered in the cavity, we get

$$U_{ac}(z)=-\frac{AH_b}{8}(z+0.5)[2({H_b}^2-3)z-({H_b}^2+1)] \quad \text{for } -1/2\leqslant z\leqslant -H_b/2,$$

$$U_{ac}(z)=-\frac{A}{16}(H_b-1)^2[4(H_b+2)z^2-H_b] \quad \text{for } -H_b/2\leqslant z\leqslant H_b/2,$$

$$U_{ac}(z)=-\frac{AH_b}{8}(z-0.5)[2({H_b}^2-3)z+({H_b}^2+1)] \quad \text{for } H_b/2\leqslant z\leqslant 1/2,$$

where $H_b=h_b/h$ is the normalized width of the acoustic source. In the case where the beam is not centered, but with its center located at $z=z_b$ ($-1/2<z_b<1/2$), we obtain

$$U_{ac}(z)=-\frac{AH_b}{8}(z+0.5)[2({H_b}^2-3+12{z_b}^2)z-({H_b}^2+1+12{z_b}^2-8z_b)] \quad \text{for } -1/2\leqslant z\leqslant z_b-H_b/2,$$

$$U_{ac}(z)=-\frac{A}{16}[4((H_b-1)^2(H_b+2)+12{z_b}^2H_b)z^2+16z_b(H_b-1)z-((H_b-1)^2H_b+4{z_b}^2(3H_b-2))] \quad \text{for } z_b-H_b/2\leqslant z\leqslant z_b+H_b/2,$$

$$U_{ac}(z)=-\frac{AH_b}{8}(z-0.5)[2({H_b}^2-3+12{z_b}^2)z+({H_b}^2+1+12{z_b}^2+8z_b)] \quad \text{for } z_b+H_b/2\leqslant z\leqslant 1/2.$$

In the case of pure buoyancy, $A=0$, and the governing equation

$$\frac{\partial^3 U_b}{\partial z^3}-\mathrm{Gr}=0 \tag{8}$$

gives the usual cubic profile

$$U_b(z)=\frac{\mathrm{Gr}}{24}(4z^3-z).$$

In the general case, the solution of the problem can be written as $U_0=U_b+U_{ac}+U'$. U' is found to verify Eq. (7)

without forcing term, which gives a quadratic profile $C(z^2-1/4)$ taking into account no slip boundary conditions. Mass conservation implies that $C=0$, and so $U'=0$ and

$$U_0(z) = U_b(z) + U_{ac}(z). \tag{9}$$

When temperature is applied, it is transported by the flow U_0 according to Eq. (6) giving rise to T_b and T_{ac} such that

$$T_0(x,z) = x + T_i(z) = x + T_b(z) + T_{ac}(z). \tag{10}$$

The part T_b induced by U_b for thermally conducting boundaries is given by

$$T_b(z) = \frac{\mathrm{Gr}\,\mathrm{Pr}}{5760}(48z^5 - 40z^3 + 7z).$$

The part T_{ac} induced by U_{ac} for thermally conducting boundaries is given in the centered case by

$$T_{ac}(z) = -\frac{\mathrm{Pr}\,AH_b}{96}(z+0.5)^3[2({H_b}^2-3)z - (3{H_b}^2-1)] \quad \text{for} \quad -1/2 \leqslant z \leqslant -H_b/2,$$

$$T_{ac}(z) = -\frac{\mathrm{Pr}\,A}{192}(H_b-1)^2\left[4(H_b+2)z^4 - 6H_b z^2 + \frac{H_b}{4}(2H_b+1)\right] \quad \text{for} \quad -H_b/2 \leqslant z \leqslant H_b/2,$$

$$T_{ac}(z) = -\frac{\mathrm{Pr}\,AH_b}{96}(z-0.5)^3[2({H_b}^2-3)z + (3{H_b}^2-1)] \quad \text{for} \quad H_b/2 \leqslant z \leqslant 1/2,$$

and when the beam is not centered by

$$T_{ac}(z) = -\frac{\mathrm{Pr}\,AH_b}{96}(z+0.5)[(z+0.5)^2(2({H_b}^2-3+12{z_b}^2)z - (3{H_b}^2-1+36{z_b}^2-16z_b)) + 4z_b(4{z_b}^2+{H_b}^2-1)] \quad \text{for} \quad -1/2 \leqslant z \leqslant z_b - H_b/2,$$

$$T_{ac}(z) = -\frac{\mathrm{Pr}\,A}{192}\left[4((H_b-1)^2(H_b+2)+12{z_b}^2H_b)z^4 + 32z_b(H_b-1)z^3 - 6((H_b-1)^2H_b + 4{z_b}^2(3H_b-2))z^2 + 8z_b(H_b-1)(4{z_b}^2 + H_b(H_b-2))z + (H_b-1)^2\frac{H_b}{4}(2H_b+1) + 8{z_b}^4 + 3{z_b}^2H_b(4H_b-3)\right] \quad \text{for} \quad z_b - H_b/2 \leqslant z \leqslant z_b + H_b/2,$$

$$T_{ac}(z) = -\frac{\mathrm{Pr}\,AH_b}{96}(z-0.5)[(z-0.5)^2(2({H_b}^2-3+12{z_b}^2)z + (3{H_b}^2-1+36{z_b}^2+16z_b)) + 4z_b(4{z_b}^2+{H_b}^2-1)] \quad \text{for} \quad z_b + H_b/2 \leqslant z \leqslant 1/2.$$

The temperature profiles T_{ac} calculated with conducting boundary conditions have zero values at the walls, but also zero second derivatives, in direct connection with Eq. (6) and the no-slip condition. Moreover, in the case of the centered beam, the first derivative of T_{ac} is also zero at the walls, which means that the expression of T_{ac} in this case is also valid for adiabatic boundary conditions. This zero heat flux value at the wall is enforced by the symmetry properties of the flow [$dT_{ac}(z)/dz$ must be odd] and heat conservation [$dT_{ac}(z)/dz$ at $z=-1/2$ must be equal to $dT_{ac}(z)/dz$ at $z=1/2$].

Some typical velocity profiles for the flows generated in the layer are shown in Figs. 2 and 3. We first present in Figs. 2(a) and 2(b) the velocity profiles created by Eckart streaming for a centered beam. They correspond to two different beam widths: $H_b=0.3$ and $H_b=0.8$. Positive velocities are obtained in the center of the layer because of the acoustic radiation pressure created by the ultrasound beam, and negative velocities corresponding to the return flow are obtained along the walls. The location of the velocity zeros is connected to the flow conservation in the section: they are outside the acoustic beam for narrow beams and inside for large beams. These velocity profiles have curvature changes at the upper and lower boundaries of the beam, and they are symmetric with respect to the center of the layer. The velocity profile generated through buoyancy by the horizontal temperature gradient [Fig. 2(c)] is the classical cubic profile with an inflection point at the center of the cavity. When the two effects are combined, the velocity profiles are more complex and have no more symmetry [Figs. 2(d) and 2(e)]. Examples of velocity profiles obtained by Eckart streaming with a noncentered beam are shown in Fig. 3. The beam width is fixed ($H_b=0.3$), but four different beam positions have been chosen. In each case, a velocity profile generated by buoyancy is given for comparison. For the positions $z_b=0.1$ [Fig. 3(b)] and $z_b=0.35$ [Fig. 3(d)], Eckart streaming generates flows which are rather opposite to those created by buoyancy (particularly for $z_b=0.35$) so that a kind of braking effect of the buoyant flow is induced by Eckart streaming. On the contrary, for the positions $z_b=-0.1$ [Fig. 3(a)] and $z_b=-0.35$ [Fig. 3(c)], Eckart streaming generates flows which are rather in the same direction as the buoyant flows, so that in these cases the buoyant flow is reinforced by Eckart streaming. Typical temperature profiles T_b and T_{ac} are also shown in Fig. 4.

III. STABILITY APPROACH

The stability of the basic flow solution [(9) and (10)] is investigated here in a general way by a linear analysis. The solution of the three dimensional problem is written as

$$(\boldsymbol{V}, P, T) = (\boldsymbol{V}_0, P_0, T_0) + (\boldsymbol{v}, p, \theta),$$

i.e., the sum of the basic flow quantities with perturbations. Substitution into Eqs. (1)–(3) and linearization with respect to the perturbations yields

$$\boldsymbol{\nabla}\cdot\boldsymbol{v} = 0, \tag{11}$$

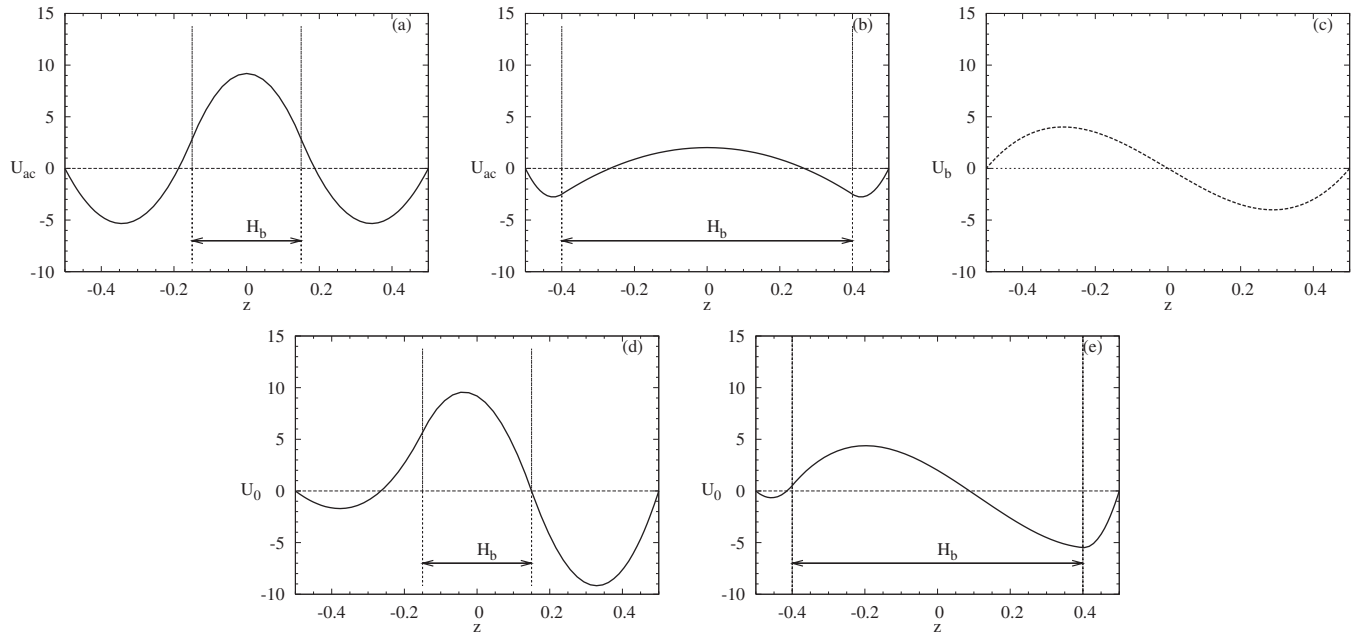

FIG. 2. Basic velocity profiles obtained for a centered ultrasound beam: flow due to the Eckart streaming for (a) $H_b=0.3$ and (b) $H_b=0.8$ ($A=1000$); flow due to the temperature gradient for (c) Gr=500 ($A=0$); flow due to the combined effect of the temperature gradient and the Eckart streaming for (d) $H_b=0.3$ and (e) $H_b=0.8$ (Gr=500, $A=1000$).

$$\frac{\partial \boldsymbol{v}}{\partial t} + (\boldsymbol{V}_0 \cdot \boldsymbol{\nabla})\boldsymbol{v} + (\boldsymbol{v} \cdot \boldsymbol{\nabla})\boldsymbol{V}_0 = -\boldsymbol{\nabla} p + \boldsymbol{\nabla}^2 \boldsymbol{v} + \mathrm{Gr}\ \theta \boldsymbol{e}_z, \tag{12}$$

$$\frac{\partial \theta}{\partial t} + \boldsymbol{V}_0 \cdot \boldsymbol{\nabla}\theta + \boldsymbol{v} \cdot \boldsymbol{\nabla} T_0 = \frac{1}{\mathrm{Pr}} \boldsymbol{\nabla}^2 \theta, \tag{13}$$

where $\boldsymbol{V}_0=(U_0,0,0)$.

Only boundary conditions in the z-direction (for $z=-1/2$ and $z=1/2$) are needed because we will use periodic disturbances in the horizontal x and y directions. These conditions are

(a) no-slip boundary conditions: $\boldsymbol{v}=0$, and

(b) conducting thermal boundary conditions: $\theta=0$.

The linear stability study consists, for fixed values of the Prandtl number Pr and acoustic streaming parameter A, in the determination of Gr_c, the critical value of Gr at which the basic flow loses its stability. For the normal modes analysis, the set of Eqs. (11)–(13) is transformed by using the following disturbances:

$$(\boldsymbol{v}, p, \theta) = (\boldsymbol{v}, p, \theta)(z) e^{i(h_x x + h_y y) + \omega t}, \tag{14}$$

where h_x and h_y are real wave numbers in the longitudinal, x, and transverse, y, directions, respectively, and $\omega=\omega_r+i\omega_i$ is a complex eigenvalue. The real part of ω represents an amplification rate and its imaginary part an oscillation frequency. These modes are elementary perturbations from which a general perturbation is obtained by superposition.

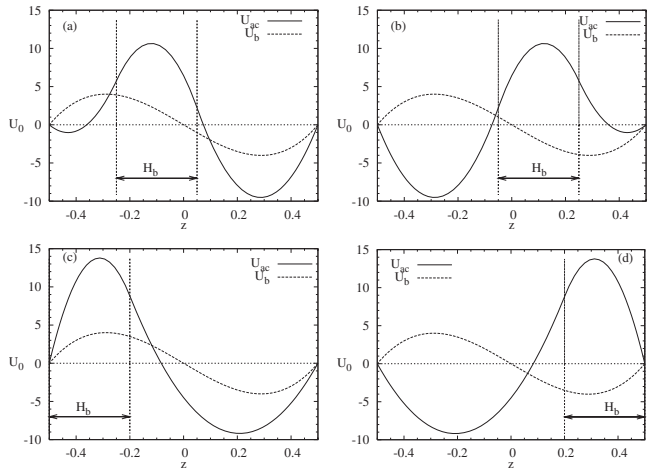

FIG. 3. Basic velocity profiles obtained for a noncentered ultrasound beam ($H_b=0.3$, $A=1000$); the velocity profiles due to Eckart streaming (U_{ac}, solid lines) are given for different beam positions, (a) $P_{1-}(z_b=-0.1)$, (b) $P_{1+}(z_b=0.1)$, (c) $P_{2-}(z_b=-0.35)$, and (d) $P_{2+}(z_b=0.35)$, and compared to the velocity profile due to the temperature gradient (U_b, dashed lines) (Gr=500).

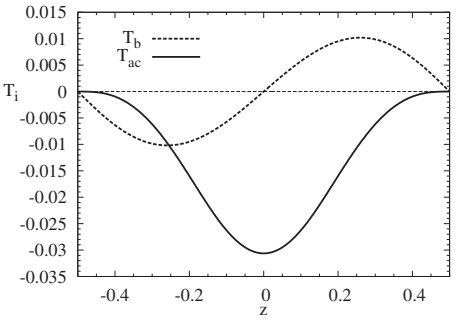

FIG. 4. Basic temperature profiles induced for Pr=0.1 by the buoyant flow (T_b, dashed line) (Gr=500) and by the Eckart streaming flow (T_{ac}, solid line) ($H_b=0.3$, $A=1000$).

An eigenvalue problem is then obtained: $LX=\omega MX$, where $X=(\boldsymbol{v}(z),p(z),\theta(z))$, L is a linear operator depending on h_x, h_y, Pr, H_b, z_b, A, and Gr, and M is a constant linear operator. This generalized eigenvalue problem is solved with the spectral Tau Chebyshev method by means of a numerical procedure using the QZ eigenvalue solver of the NAG library [22]. From the thresholds $\mathrm{Gr}_0(\mathrm{Pr},H_b,z_b,A,h_x,h_y)$ (values of Gr for which an eigenvalue has a real part equal to zero whereas all the other eigenvalues have negative real parts), the critical Grashof number Gr_c can be obtained after minimization along h_x and h_y. In fact, Gr_c was obtained for perturbations where either h_x or h_y was equal to zero, i.e., pure longitudinal or transverse waves. It is known that in the pure thermal case, there is no smaller minimum for perturbations with both $h_x\neq 0$ and $h_y\neq 0$ [23]. We have verified to our best that it is the same in our situation.

The critical Grashof numbers were determined by expanding the variables in the z direction in a Chebyshev series with 80 collocation points. In fact, 20–30 collocation points were sufficient for an accurate determination of the linear stability characteristics for the pure buoyancy case ($A=0$), but more points were necessary when acoustic streaming is effective because of the strong gradients generated at the limits of the acoustic beam. Note that in the pure acoustic streaming situation, the critical parameter is the acoustic streaming parameter A, but the determination of its critical value is similar to what has been explained for Gr. In the following, we will first consider the stability of the pure acoustic streaming flow and then study the effect of the acoustic streaming on the stability of the laterally heated layer.

IV. STABILITY RESULTS FOR THE PURE ACOUSTIC STREAMING FLOW

The flows considered in this section are those created by Eckart streaming in a layer. Typical velocity profiles for these flows (denoted as U_{ac}) have been shown in Figs. 2(a) and 2(b) (centered beam) and Fig. 3 (noncentered beam). In these cases, the linear stability analysis gives the critical value of the acoustic streaming parameter, A_c, above which the acoustic streaming flow becomes unstable. Results have first been obtained in the case of a centered acoustic beam for different beam widths H_b, and then, at constant beam width, for different positions of the beam across the layer.

The critical stability curve giving the evolution of A_c as a function of H_b for a centered beam is shown in Fig. 5(a). These thresholds correspond to two-dimensional instabilities ($h_x\neq 0$, $h_y=0$) developing in the plane of the basic flow profile (plane xOz). The critical curve separates the stable zone (small values of A) and the unstable zone (large values of A). The influence of the beam width on the thresholds is found to be strong. The critical curve has a minimum, $A_c=5143$, for $H_b\approx 0.32$, which means that the acoustic streaming flow obtained with such a beam width is the more unstable (the associated critical parameters are $h_{x_c}=4.5$ and $\omega_c=21$). [This value of H_b is close to, but smaller than the values which give either the maximum velocity variation ($U_{max}-U_{min}$) ($H_b=0.388$) or the maximum shear ($H_b=0.366$) in the basic velocity profile.] The thresholds increase for both smaller and higher values of H_b. The increase for large H_b is particularly strong, indicating that the streaming flows induced by large width beams (close to the height of the layer) are particularly stable. The two-dimensional instability involved in these streaming flows is hydrodynamic: the basic velocity profile is symmetric with two shear zones at the limits of the acoustic beam (see Fig. 2) which destabilize the flow. These shear zones move toward the walls when H_b is increased. The instability is oscillatory and associated with a single complex eigenvalue (no complex conjugate eigenvalue). The critical angular frequency is positive, indicating a right traveling wave. This frequency is weak for small values of H_b and increases with H_b [Fig. 5(c)]. This increase becomes very strong beyond $H_b=0.6$, which leads to high oscillation frequencies for the large beam widths. The variation of the critical wave number h_{x_c} is shown in Fig. 5(b). h_{x_c} decreases as H_b is increased, which corresponds to an evolution toward larger wavelengths for the instabilities. This decrease is almost linear for $0\leqslant H_b\leqslant 0.6$ but becomes steeper when H_b is further increased.

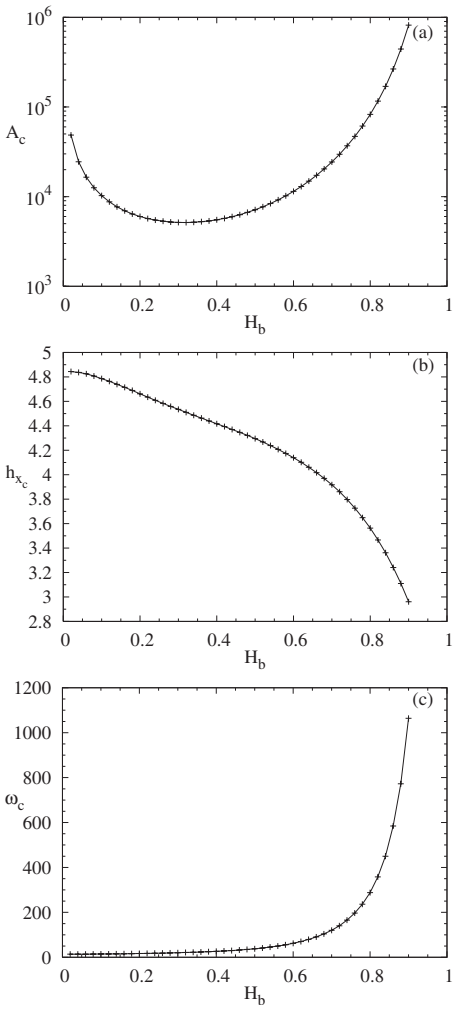

FIG. 5. (a) Critical acoustic streaming parameter A_c, (b) wave number h_{x_c}, and (c) angular frequency ω_c as a function of the acoustic beam width H_b for an isothermal layer and a centred acoustic beam. In (a), the flow is unstable above the curve and stable below the curve.

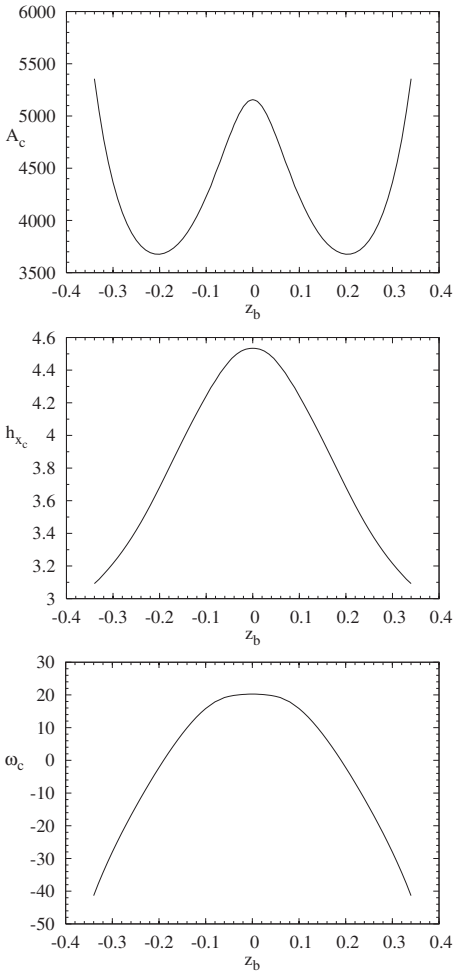

FIG. 6. (a) Critical acoustic streaming parameter A_c, (b) wave number h_{x_c}, and (c) angular frequency ω_c as a function of the position of the beam center z_b for an isothermal layer and a fixed beam width $H_b=0.3$. Identical results are obtained for a decentring towards the top of the layer ($z_b>0$) and a decentring towards the bottom ($z_b<0$).

We now consider that the acoustic beam has a fixed width ($H_b=0.3$), but that its position inside the layer is changed. Figure 6(a) shows the variation of the critical thresholds A_c as a function of the position of the beam center z_b. We see that for opposite positions of the beam ($z_b=\pm k$), the same thresholds A_c are obtained. This is due to the fact that the flows obtained are symmetric one of the other with respect to the center of the layer and are thus completely equivalent. For $z_b=0$, the threshold is that found previously for a centered beam. When the beam is moved away from the center, the thresholds A_c first decrease, until the positions $|z_b\approx 0.2|$ beyond which they increase. These instabilities are oscillatory, and, as shown in Fig. 6(c), the critical angular frequency ω_c evolves with $|z_b|$ from the positive value obtained for a centered beam toward negative values which are reached for $|z_b|>0.18$. This change of sign corresponds to a transition from right to left traveling waves. It occurs at positions of the beam which are close to those corresponding to the minimum values of the thresholds. The critical wave number of the instabilities, h_{x_c}, decreases monotonically when $|z_b|$ increases, i.e., when the beam gets closer to the walls.

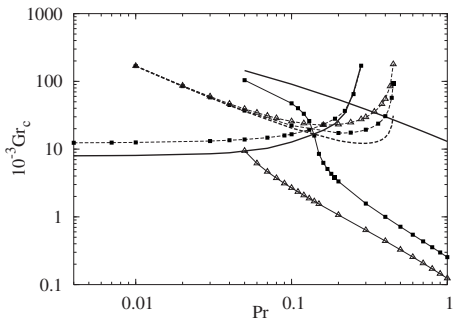

FIG. 7. Critical Grashof number Gr_c for the three dominant instabilities as a function of the Prandtl number Pr for a centered beam with $H_b=0.8$ and different values of the acoustic streaming parameter, $A=0$ (thick lines), 5×10^4 (lines with squares), and 10^5 (lines with circles). Solid curves correspond to steady thresholds and dashed lines to oscillatory thresholds.

Note that we have also considered the case where the perturbations are three dimensional ($h_y\neq 0$). In any case, the thresholds have been found larger than those obtained for $h_y=0$. In particular, for $h_y\neq 0$ and $h_x=0$ (i.e. when the instabilities develop in the transverse yOz plane), no finite thresholds have been found, which corresponds to eigenvalues with always negative real parts. The acoustic streaming flow is then linearly stable with respect to these three-dimensional perturbations with $h_x=0$, this result being valid for any positions of the beam.

V. STABILITY RESULTS FOR THE LATERALLY HEATED FLUID LAYER SUBJECT TO ACOUSTIC STREAMING

In this section, we will study the effect of acoustic streaming on the linear stability of the flow induced in a fluid layer by a horizontal temperature gradient. In the pure buoyancy situation, i.e., without acoustic streaming [see the velocity profile in Fig. 2(c)], steady two-dimensional instabilities of dynamical origin (transverse rolls) prevail for very small Prandtl number values (typically, $\mathrm{Pr}\leqslant 0.14$), whereas oscillatory and then steady three-dimensional instabilities (longitudinal rolls) prevail when the Prandtl number is further increased. These instability thresholds are shown as thick lines in Fig. 7 for $0.004\leqslant \mathrm{Pr}\leqslant 1$. We will first see how the instability thresholds in this Pr range globally evolve with acoustic streaming. We will then more precisely analyze the influence of acoustic streaming on the different instabilities at fixed values of Pr.

A. Global effect of acoustic streaming on the thresholds

The global effect of acoustic streaming on the thresholds of the different instabilities is presented in Fig. 7 for a beam width $H_b=0.8$ and for two values of the acoustic streaming parameter, $A=5\times 10^4$ and 10^5. The two-dimensional instabilities obtained in the domain of low Prandtl numbers are steady for $A=0$, but they become oscillatory as soon as acoustic streaming is applied. For these instabilities, an in-

crease of the thresholds is found for $A=5\times10^4$. There is, however, a limitation of the acoustic streaming parameter in this case due to the destabilization of the pure acoustic streaming flow for $A_c=82\,641$. The thresholds of the oscillatory three-dimensional instabilities also increase with the acoustic streaming parameter A. This increase is quite strong for $0.2\leqslant \mathrm{Pr}\leqslant 0.4$; it decreases for smaller values of Pr and becomes negligible for $\mathrm{Pr}\leqslant 0.05$. The effect of acoustic streaming is the strongest on the steady three-dimensional instabilities, but it is now a decrease of the thresholds which is found when A is increased. A monotonous effect of the acoustic streaming is thus found for the three-dimensional instabilities, i.e., an increase of the oscillatory thresholds and a decrease of the steady thresholds. This corresponds to a stabilization of the basic flow with respect to the oscillatory instabilities and a destabilization with respect to the steady instabilities.

B. Effect of acoustic streaming on the different instabilities at fixed Pr

We now focus on the precise evolution of the thresholds Gr_c as we vary the acoustic streaming parameter A and the beam width H_b at fixed values of the Prandtl number. We will calculate the thresholds of the two-dimensional instability for $\mathrm{Pr}=0.01$ and those of the three-dimensional instabilities for $\mathrm{Pr}=0.1$. In each case, we will first consider the situation where the acoustic beam, of variable width ($0.1\leqslant H_b \leqslant 0.8$), is centered, and then, for $H_b=0.3$, we will consider the effect obtained when the acoustic beam is decentered.

1. *Steady two-dimensional instabilities for* Pr=0.01

The action of acoustic streaming on the two-dimensional instabilities is shown for a centered beam in Fig. 8(a) through the critical curves giving the evolution of Gr_c with A for different values of H_b. For $A=0$ (no acoustic effect), the flow is thermally induced, and the instability is steady and appears for $\mathrm{Gr}_c=8076$. The evolution of Gr_c with A depends on the acoustic beam width H_b. For values of H_b lower than 0.6, Gr_c continuously decreases with the increase of A, indicating a destabilizing influence of acoustic streaming, whereas for values of H_b greater than 0.6, Gr_c first increases with the increase of A, then reaches a maximum, and eventually decreases. For large acoustic beam widths, it is then possible to find a range of acoustic streaming parameter values where acoustic streaming has a stabilizing influence on the basic thermally induced flow. The extent of this parameter range and the stabilizing effect induced increase with the increase of the beam width. In any case, the curves of Gr_c eventually decrease to zero. The value $\mathrm{Gr}_c=0$ is reached for values of A which, as expected, are those already obtained in the pure acoustic streaming situation [Fig. 5(a)]. The instability seems hydrodynamic as it evolves, with the increase of A, from an instability connected to the shear of the thermally induced flow in the center of the layer, toward an instability connected to the shear of the acoustic streaming flow at the limits of the acoustic beam.

The curves giving the evolution of the critical wavelength h_{x_c} with A are shown in Fig. 8(b). An increase of h_{x_c} is

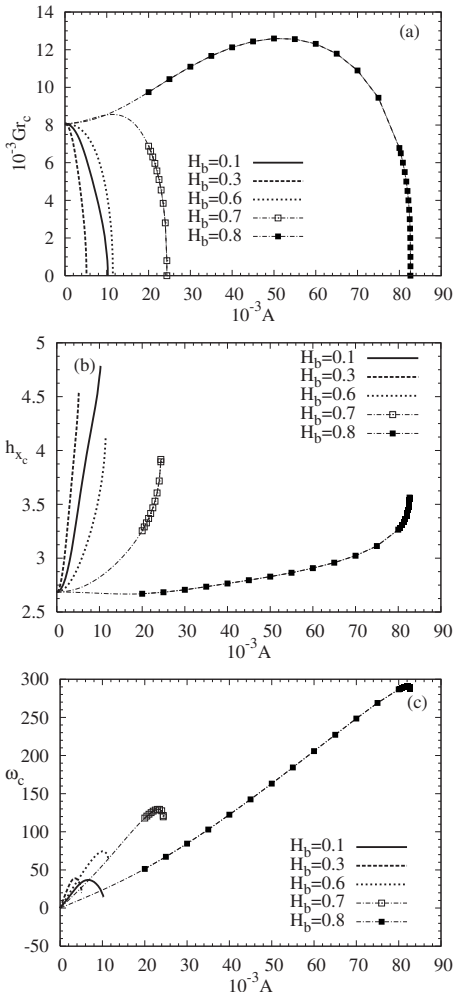

FIG. 8. (a) Critical Grashof number Gr_c, (b) wave number h_{x_c}, and (c) angular frequency ω_c for the two-dimensional instabilities as a function of the acoustic streaming parameter A for a centered beam of different widths H_b and $\mathrm{Pr}=0.01$. The critical curves in (a) intersect the axis $\mathrm{Gr}=0$ at values of A which are the critical values shown in Fig. 5(a).

observed, from $h_{x_c}=2.68$ corresponding to the pure buoyancy situation ($A=0$) to the values of h_{x_c} corresponding to the pure acoustic streaming situation ($A=A_c$). This increase is continuous, except for $H_b=0.8$ (case with the strongest stabilization) where a slight initial decrease is found.

Finally, as shown in Fig. 8(c), the critical angular frequency ω_c (which is zero for $A=0$) strongly increases with A until a maximum is reached and then decreases down to the value corresponding to the pure acoustic streaming situation. The maximum value reached by ω_c increases with the acoustic beam width H_b. These curves show that the two-dimensional instabilities become oscillatory as soon as acoustic streaming is applied. Moreover, the positive values of ω_c indicate the onset of right traveling waves in these cases.

The influence of the beam position on the thresholds of the two-dimensional instabilities is shown in Fig. 9(a). This figure displays the variation of Gr_c with the acoustic streaming parameter A for a beam of fixed width $H_b=0.3$ located at

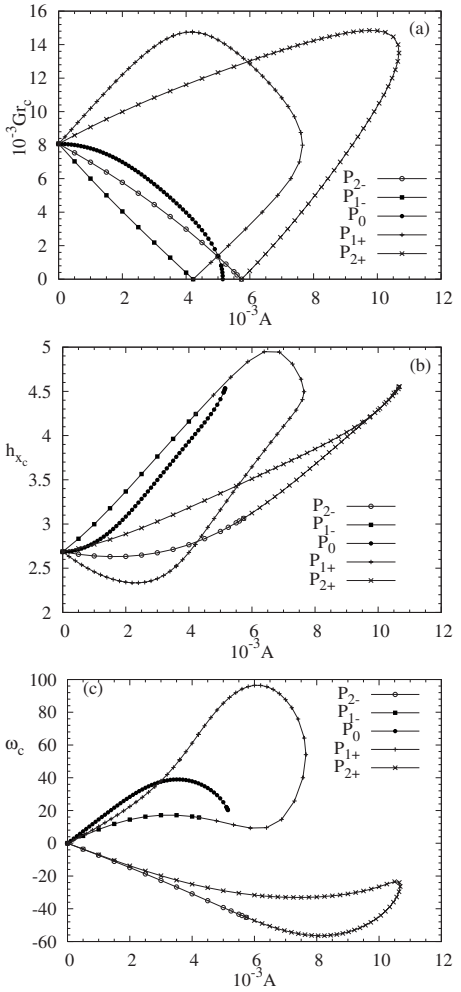

FIG. 9. (a) Critical Grashof number Gr_c, (b) wave number h_{x_c}, and (c) angular frequency ω_c for the two-dimensional instabilities as a function of the acoustic streaming parameter A for different positions of the ultrasound beam [$P_{2-}(z_b=-0.35)$, $P_{1-}(z_b=-0.1)$, $P_{1+}(z_b=0.1)$, and $P_{2+}(z_b=0.35)$]. The beam width is equal to $H_b=0.3$ and Pr=0.01. The stable zone in (a) is the zone delimited by a critical curve and containing the origin. The critical curves in (a) intersect the axis Gr=0 at values of A which are the critical values shown in Fig. 6(a) (same values for opposite z_b).

different positions inside the layer. The results obtained for a centered beam [position $P_0(z_b=0)$] are compared with those obtained for symmetric positions with respect to the center of the layer, $P_{1-}(z_b=-0.1)$, $P_{1+}(z_b=0.1)$ and $P_{2-}(z_b=-0.35)$, $P_{2+}(z_b=0.35)$. Note that all the thresholds are oscillatory, except, indeed, for $A=0$. Figure 9 highlights the strong influence of the beam position. For the positions $P_{1-}(z_b=-0.1)$ and $P_{2-}(z_b=-0.35)$, where acoustic streaming rather reinforces the thermally induced flow [see Figs. 3(a) and 3(c)], the thresholds decrease monotonically with A as for the centered position of the beam, but more quickly, and they reach $Gr_c=0$ at the values of A_c already obtained in the pure acoustic streaming situation [Fig. 6(a)]. For these positions, the acoustic streaming strongly destabilizes the basic flow. On the contrary, for the positions $P_{1+}(z_b=0.1)$ and $P_{2+}(z_b=0.35)$ where acoustic streaming rather opposes the thermally induced flow [see Figs. 3(b) and 3(d)], the thresholds

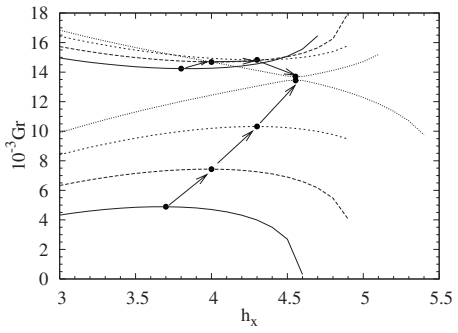

FIG. 10. Neutral curves Gr_0 for the two-dimensional instabilities as a function of the wavenumber h_x for the beam position $P_{2+}(z_b=0.35)$ and different values of the acoustic streaming parameter, $A=8000$, 9000, 10 000, and 10 678 (following the arrows). The beam width is equal to $H_b=0.3$ and Pr=0.01. For each value of A, two neutral curves are obtained. The black dots indicate the minima or maxima of these neutral curves, i.e., the critical thresholds Gr_c shown in Fig. 9(a).

first increase with the increase of A which indicates a stabilization of the basic flow by acoustic streaming. The critical curves then reach a maximum and decrease down to the values of A_c for pure acoustic streaming [the same values as for the symmetric positions, as already shown in Fig. 6(a)]. These critical curves, however, have a particular shape: indeed, they evolve until values of A larger than A_c (up to a limit value A_l) so that the last portion of curve is associated with decreasing values of A. Moreover, the stable zone in these cases is the zone delimited by the critical curve and containing the origin. A specific evolution is then induced when Gr is increased for values of A larger than A_c and smaller than A_l. The flow, first unstable for the small values of Gr, is stabilized beyond a first threshold and becomes again unstable beyond a second threshold. This behavior is depicted in Figs. 10 and 11 for the position P_{2+} of the acoustic beam. Figure 10 shows the neutral curve Gr_0 as a function of the wave number h_x for different values of A, $A=8000$, 9000, 10 000, and 10 678, the last value being close to the disappearance of the critical curve. For each value of A, two

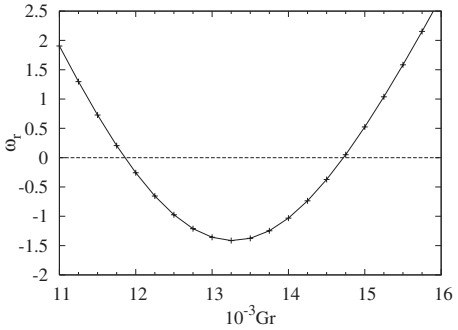

FIG. 11. Real part of the dominant eigenvalue, ω_r, as a function of the Grashof number Gr for the beam position $P_{2+}(z_b=0.35)$, $A=10\,500$, and $h=4.48$. The beam width is equal to $H_b=0.3$ and Pr=0.01. The two Gr values associated to zero ω_r belong to neutral curves as those shown in Fig. 10, and the negative values of ω_r in between indicate the stability of the zone between the neutral curves.

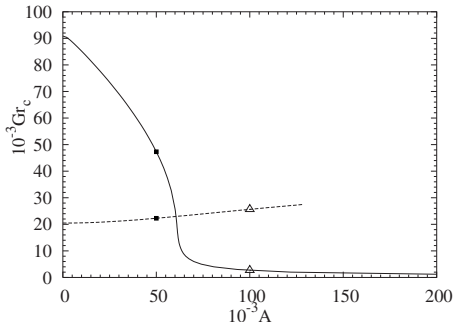

FIG. 12. Critical Grashof number Gr_c for the steady (solid curve) and oscillatory (dashed curve) three-dimensional instabilities as a function of the acoustic streaming parameter A for a centered beam with $H_b=0.8$ and Pr=0.1.

neutral curves are obtained, an upper convex curve above which instability is triggered and where Gr_c appears as a minimum, and a lower concave curve below which instability is triggered and where Gr_c appears as a maximum. Between these curves, there exists indeed a stable zone, which is confirmed by the plot of the dominant eigenvalue as a function of Gr for $A=10\,500$ and $h=4.48$ in Fig. 11 where we see that the real part of this dominant eigenvalue becomes negative in an intermediate range of Gr values. Moreover, Fig. 10 clearly shows that the stable zone shrinks as A is increased and eventually disappears when the minimum of the convex curve becomes smaller than the maximum of the concave curve.

Finally, Figs. 9(b) and 9(c), respectively, depict the variations of the critical wave number h_{x_c} and angular frequency ω_c as a function of the acoustic streaming parameter A. We see that the critical curves obtained for symmetric positions of the beam join at values of h_{x_c} and ω_c corresponding to the pure acoustic streaming situation. Figure 9(c) confirms that, except for $A=0$, all the thresholds are oscillatory. ω_c evolves toward positive values for the position P_0 (centered beam) and the positions P_{1-} and P_{1+} ($|z_b|=0.1$) indicating the onset of right traveling waves, whereas it evolves towards negative values for the positions P_{2-} and P_{2+} ($|z_b|=0.35$) indicating the onset of left traveling waves. Note the strong increase of the angular frequency for the position P_{1+} of the acoustic beam corresponding to $z_b=0.1$.

2. *Three-dimensional instabilities for* Pr=0.1

The effect of acoustic streaming on the thresholds of the three-dimensional instabilities is first shown for $H_b=0.8$ and Pr=0.1 and for a centered acoustic beam in Fig. 12. For $A=0$, two instabilities are found: an oscillatory instability corresponding to a pair of complex conjugate eigenvalues (onset of a symmetry degenerate left or right traveling wave) which appears for $Gr_c=20\,466$ and a steady instability which appears much later for $Gr_c=91\,000$. For small values of A, the oscillatory thresholds, slightly increasing, are indeed the true critical thresholds. The steady thresholds, however, which were very high for $A=0$, strongly decrease with the increase of A and eventually become the true critical thresholds beyond a value of A which, for $H_b=0.8$ and Pr=0.1, is estimated at around 60 000. This crossing of the oscillatory and steady thresholds is highlighted for different values of H_b and Pr=0.1 in Fig. 13(a) where only the lower thresholds are plotted. We see that, for $0.3\leqslant H_b\leqslant 0.8$, the value of A at which the transition occurs increases with H_b, whereas the corresponding value of Gr_c is almost constant, around $Gr_c=23\,000$. For values of A below the transition, the oscillatory thresholds slightly increase with A, for any value of H_b, confirming the stabilizing effect of acoustic streaming on the oscillatory three-dimensional instability. For values of A above the transition, we observe that, for any value of H_b, the steady thresholds decrease very strongly with the increase of A and go asymptotically to zero as A^{-1}, which confirms the stability of the pure acoustic streaming flows (Gr=0) with respect to three-dimensional instabilities.

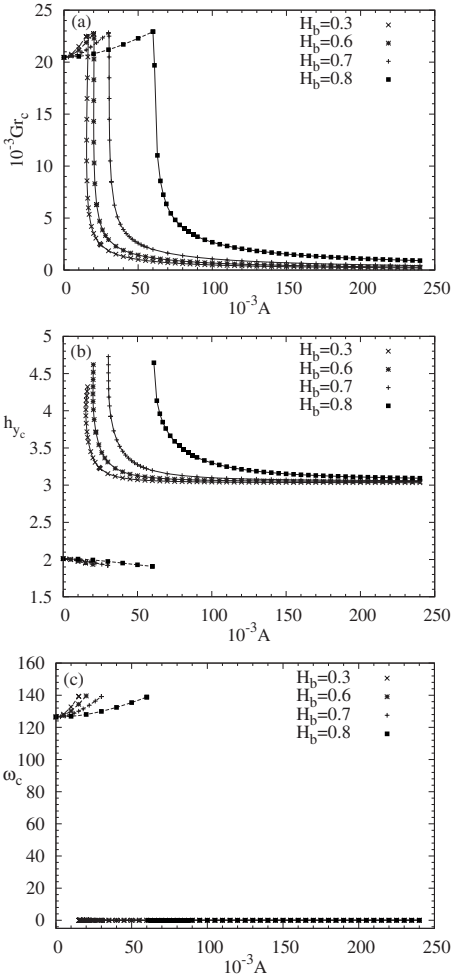

FIG. 13. (a) Critical Grashof number Gr_c, (b) wave number h_{y_c}, and (c) angular frequency ω_c for the steady (solid curve) and oscillatory (dashed curve) three-dimensional instabilities as a function of the acoustic streaming parameter A for a centered beam of different widths H_b and Pr=0.1. Only the portions of the critical curves corresponding to the first threshold are shown. The stable zone in (a) is the zone delimited by a critical curve and containing the origin.

The critical wave number h_{y_c} and angular frequency ω_c of these three-dimensional instabilities are depicted in Figs. 13(b) and 13(c). The critical angular frequency of the oscillatory instability (which is still associated with a pair of com-

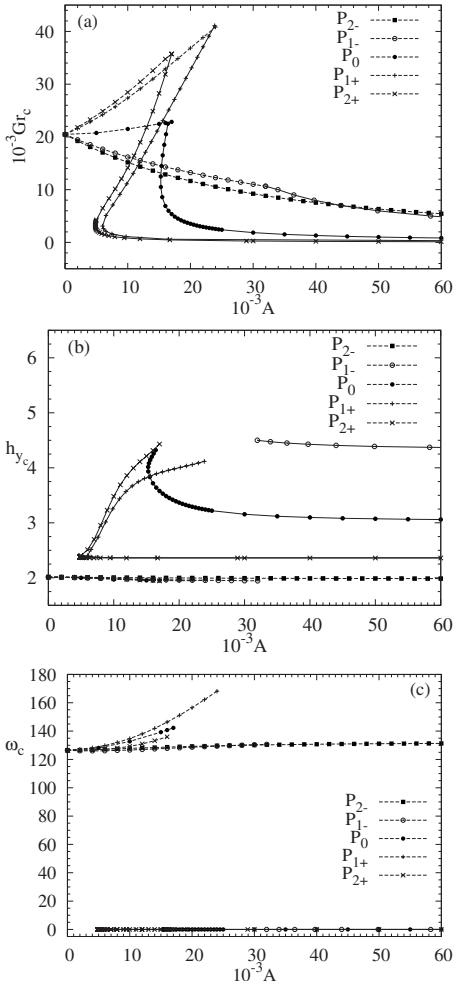

FIG. 14. (a) Critical Grashof number Gr_c, (b) wave number h_{y_c}, and (c) angular frequency ω_c for the steady (solid curve) and oscillatory (dashed curve) three-dimensional instabilities as a function of the acoustic streaming parameter A for different positions of the ultrasound beam [$P_{2-}(z_b=-0.35)$, $P_{1-}(z_b=-0.1)$, $P_{1+}(z_b=0.1)$, and $P_{2+}(z_b=0.35)$]. The beam width is equal to $H_b=0.8$ and Pr=0.1. Only the portions of the critical curves corresponding to the first threshold are shown. The stable zone in (a) is the zone (for $Gr \geqslant 0$) delimited by a critical curve and containing the origin.

plex conjugate eigenvalues) slightly increases with A, in a similar way as the critical thresholds. For larger values of A, the instability is steady and $\omega_c=0$. The critical wave number h_{y_c} is almost constant (around 2) for the oscillatory instability, whereas it is stronger but decreases with the increase of A for the steady instability and asymptotically approaches a limiting value (close to $h_{y_c}=3$) which seems independent of the beam width H_b.

The influence of the beam position on the thresholds of the three-dimensional instabilities is shown in Fig. 14(a). The beam width and beam positions are the same as those already used for the two-dimensional instabilities in Fig. 9(a). The displacement of the beam has different consequences on the oscillatory and steady three-dimensional instabilities. Compared to the centered position P_0, the positions P_{1+} and P_{2+}, which strongly stabilized the two-dimensional instabilities, also stabilize the oscillatory three-dimensional instabilities, but they induce a steeper decrease of the thresholds of the steady three-dimensional instabilities. In contrast, for the positions P_{1-} and P_{2-}, we get a destabilizing effect for the oscillatory three-dimensional instabilities, whereas the steady thresholds decrease more slowly.

We now consider the global effect of the beam position on the true critical thresholds of the three-dimensional instabilities. For the positions P_{1+} and P_{2+}, the stable zone extends until larger values than in the centered case: for the position P_{2+}, for example, values of Gr around 42 000 are reached, whereas, in the centered case, for any beam width Gr is less than 23 000. This would show that, to get a better stabilization, it is better to adequately move the beam than to increase its width. This stable zone, however, has a particular shape so that both values of A and Gr have to be adjusted to get a stabilizing effect. When A is too strong, above a limiting value which decreases when Gr gets smaller, the flow becomes unstable with respect to the steady three-dimensional instability which is triggered for very small values of Gr_c. For the positions P_{1-} and P_{2-}, the stable zone reaches smaller values of Gr_c than in the centered case, but it extends until larger values of A because of the slower decrease of the steady three-dimensional instability thresholds. Besides, for the position P_{1-}, because of this weak decrease, only the oscillatory three-dimensional instability is involved in the critical thresholds in the range of A shown ($A \leqslant 60\,000$).

Finally, Figs. 14(b) and 14(c), respectively, depict the variations of the critical wave number h_{y_c} and angular frequency ω_c as a function of the acoustic streaming parameter A. We see that for any position of the beam, the wave number for the oscillatory instability is almost constant and close to $h_{y_c}=2$. In contrast, the wave number for the steady instability depends on both the beam position and A. For large A, h_{y_c} asymptotically tends to a limiting value which depends on the beam position (note however that the positions P_{1+} and P_{2+} give the same limiting value). Concerning the angular frequency, it increases with A, but this increase depends on the beam position.

VI. ENERGY ANALYSES

In order to better understand the stabilizing or destabilizing mechanisms which affect the convective flows when acoustic streaming is applied, we performed energy analyses for the different instabilities involved. The equations of energy budget associated with the fluctuating kinetic energy and thermal energy can be derived from the linear stability equations (12) and (13): Eq. (12) is multiplied by $\boldsymbol{v}^*$, Eq. (13) by θ^*, and the real parts of the resulting equations are taken (Re and the superscript $*$ denote the real part and the complex conjugate, respectively).

The equation expressing the rate of change of the fluctuating kinetic energy (defined as $k=\boldsymbol{v}\boldsymbol{v}^*/2$) is given by

$$\frac{\partial k}{\partial t} = \omega_r(uu^* + vv^* + ww^*) = k_s + k_d + k_b + k_p, \qquad (15)$$

where $k_s=\mathrm{Re}(-w\frac{\partial U_0}{\partial z}u^*)$ represents the production of fluctuating kinetic energy by shear of the basic flow, $k_d=\mathrm{Re}[-(h_x^2$

$+h_y^2)(uu^*+vv^*+ww^*)+\frac{\partial^2 u}{\partial z^2}u^*+\frac{\partial^2 v}{\partial z^2}v^*+\frac{\partial^2 w}{\partial z^2}w^*]$ represents the viscous dissipation of fluctuating kinetic energy, $k_b=\mathrm{Re}(\mathrm{Gr}\,\theta w^*)$ represents the production of fluctuating kinetic energy by buoyancy, and $k_p=-\mathrm{Re}[(ih_x u^*+ih_y v^*)p+\frac{\partial p}{\partial z}w^*]$ represents the redistribution of fluctuating kinetic energy by the pressure fluctuations. We can also define the total (or volume integral) fluctuating kinetic energy as $K=\int_z k dz$. The rate of change of K is given by an equation similar to Eq. (15), which involves the volume integral energy terms (denoted by K),

$$\frac{\partial K}{\partial t}=K_s+K_d+K_b. \tag{16}$$

Note that the volume integral pressure term is zero and has therefore not been included in Eq. (16). At threshold, the critical eigenvector is associated with an eigenvalue of zero real part. This implies that $\partial k/\partial t$ and $\partial K/\partial t$ are both equal to zero at marginal stability. K_d is stabilizing by nature and is thus a negative term. We choose to decompose K_d in two contributions such that $K_d=K_{d\|}+K_{d\perp}$ (similarly, we can write $k_d=k_{d\|}+k_{d\perp}$). $K_{d\|}$ is the contribution involving the velocity components in the plane of the perturbation (plane xOz for the two-dimensional instabilities and plane yOz for the three-dimensional instabilities) and $K_{d\perp}$ is the contribution related to the direction perpendicular to this plane. The kinetic energy equations are then normalized by $|K_{d\|}|$. At threshold, and if the normalized terms are denoted with a prime, we get

$$k_s'+k_{d\perp}'+k_{d\|}'+k_b'+k_p'=0, \tag{17}$$

and

$$K_s'+K_{d\perp}'+K_b'=1. \tag{18}$$

Finally, according to Eq. (9), the basic flow can be decomposed in its buoyant and acoustic parts, these two parts being proportional to Gr and A, respectively. We can then write $U_0=U_b+U_{ac}=\mathrm{Gr}\,U_{b0}+AU_{ac0}$, which allows to write the shear terms as $k_s'=k_{s_b}'+k_{s_{ac}}'=\mathrm{Gr}\,k_{s_b}''+Ak_{s_{ac}}''$ and $K_s'=K_{s_b}'+K_{s_{ac}}'=\mathrm{Gr}\,K_{s_b}''+AK_{s_{ac}}''$.

The equation expressing the rate of change of the fluctuating thermal energy (defined as $e=\theta\theta^*/2$) is given by

$$\frac{\partial e}{\partial t}=\omega_r(\theta\theta^*)=e_v+e_h+e_d, \tag{19}$$

where $e_v=-\mathrm{Re}(w\frac{\partial T_0}{\partial z}\theta^*)$ represents the production of fluctuating thermal energy by vertical transport of temperature, $e_h=-\mathrm{Re}(u\frac{\partial T_0}{\partial x}\theta^*)$ represents the production of fluctuating thermal energy by horizontal transport of temperature, and $e_d=\mathrm{Re}[\frac{1}{\mathrm{Pr}}(-(h_x^2+h_y^2)\theta+\frac{\partial^2\theta}{\partial z^2})\theta^*]$ represents the dissipation of fluctuating thermal energy by conduction. We can also define the total fluctuating thermal energy as $E=\int_z e dz$. The rate of change of E is given by an equation similar to Eq. (19), which involves the volume integral energy terms (denoted by E),

$$\frac{\partial E}{\partial t}=E_v+E_h+E_d. \tag{20}$$

At threshold, and with a normalization with respect to $|E_d|$, we get

$$e_v'+e_h'+e_d'=0, \tag{21}$$

and

$$E_v'+E_h'=1. \tag{22}$$

According to Eq. (10), E_v' can also be split in two terms related to buoyancy and acoustic streaming, respectively, which gives: $E_v'=E_{v_b}'+E_{v_{ac}}'$.

For any instability at its critical threshold, the calculation of all the individual total energy contributions [Eqs. (18) and (22)] by using the corresponding critical eigenvector enables us to determine which term plays a dominant role in triggering the instability through production of fluctuating energy. The corresponding spatial fields [Eqs. (17) and (21)] can in turn be analyzed to locate the production regions.

In the case of the two-dimensional instabilities (considered for Pr=0.01), we will analyze two cases, the case $H_b=0.3$ where acoustic streaming has a destabilizing influence and the case $H_b=0.8$ where acoustic streaming has a stabilizing influence in a large range of A. In the case of the three-dimensional instabilities (considered for Pr=0.1), we saw that the results do not depend much on H_b and that acoustic streaming has only a weak influence on the oscillatory instabilities. As a consequence, we will only analyze the steady three-dimensional instabilities and choose a given beam width, $H_b=0.8$. All these analyses will be performed for a centered acoustic beam.

A. Energy budgets for the two-dimensional instability

We recall that without acoustic streaming, the two-dimensional instability is connected to the shear of the basic flow at the center of the fluid layer, and the temperature fluctuations will play a negligible role, particularly for the small values of Pr as Pr=0.01. As a consequence, we will only consider the kinetic energy budgets in this case, and we will analyze how these budgets evolve when the acoustic streaming parameter A is increased for the two beam widths, $H_b=0.3$ and $H_b=0.8$. For this two-dimensional instability, there is no velocity perturbation in the transverse direction y which implies that $K_d=K_{d\|}$, $K_{d\perp}'=0$, $k_d'=k_{d\|}'$, and $k_{d\perp}'=0$.

1. Total energy budgets

For $H_b=0.3$ (destabilizing influence of acoustic streaming), the evolution with A of the different terms of the total kinetic energy budget is shown in Fig. 15(a). We see that whatever is A, the shear term K_s' is the dominant destabilizing term with values close to 1 indicating that this term almost balances the dissipation term. The buoyancy term K_b' is very weak: slightly stabilizing for $A=0$, it goes to 0 when the instability is purely acoustic at $A=A_c=5152$. The decomposition of the shear term K_s' shows that with the increase of A the system evolves from an instability due to the shear of the

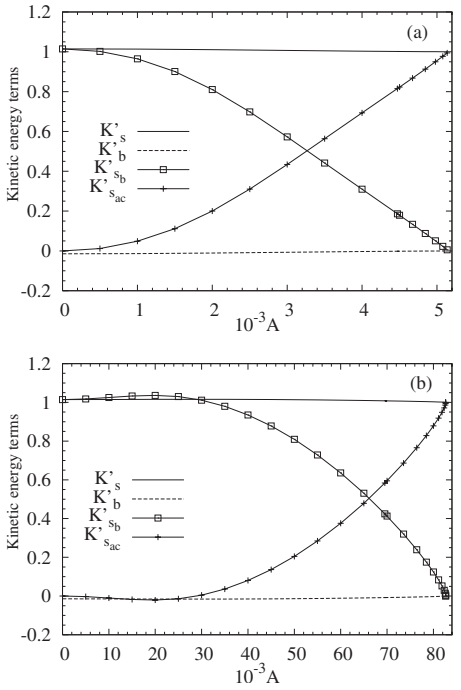

FIG. 15. Variation of the different terms of the total fluctuating kinetic energy budget (K'_b, K'_s, K'_{s_b}, and $K'_{s_{ac}}$) for the two-dimensional instabilities at threshold as a function of the acoustic streaming parameter A for (a) $H_b=0.3$ and (b) $H_b=0.8$. The beam is centered and Pr=0.01.

buoyancy generated flow, K'_{s_b}, to an instability due to the shear of the acoustic streaming flow, $K'_{s_{ac}}$. This transition is very regular, with a continuous increase of $K'_{s_{ac}}$ from 0, associated with a continuous decrease of K'_{s_b} which reaches 0 at $A=A_c=5152$.

For $H_b=0.8$ (stabilizing influence of acoustic streaming), the evolution with A of the different terms of the total kinetic energy budget is shown in Fig. 15(b). As for $H_b=0.3$, the shear term K'_s, around 1, is responsible for the destabilization and the stabilizing buoyancy term is very weak. The main difference concerns the evolution of the shear contributions, K'_{s_b} and $K'_{s_{ac}}$. $K'_{s_{ac}}$ is first slightly negative, indicating an initial stabilizing effect, before a strong increase. Correspondingly, K'_{s_b} slightly increases before the strong decrease leading to 0 at $A=A_c=82\,641$. The maximal stabilizing effect of $K'_{s_{ac}}$ (which corresponds to the maximal destabilizing effect of K'_{s_b}) is obtained for $A\approx 20\,000$, and the strong evolutions of these terms are only observed beyond $A=30\,000$ which roughly corresponds to the end of the stabilizing effect of $K'_{s_{ac}}$.

2. Local energy budgets and structure of the perturbations

For the two cases $H_b=0.3$ and $H_b=0.8$, we will analyze the spatial structure of the different fluctuating kinetic energy contributions in connection with the spatial structure of the basic flow and perturbations. The analysis will be performed at the thresholds of the two-dimensional instability for selected values of A.

The plots of the basic velocity profile $U_0(z)$, the z profiles of the local energy contributions (k'_s, k'_d, k'_b, and k'_p), and the perturbation velocity field in the vertical longitudinal xOz plane are shown in Fig. 16 for $H_b=0.3$ and $A=0$, 4000, and $A=A_c=5152$. We first see the progressive modification of the basic flow as A is increased, from the classical cubic profile of the side-heated flow toward the symmetric, piecewise parabolic profile of acoustic streaming. Concerning the energy contributions, for $A=0$ we see the strong destabilizing contribution of the shear at the center of the layer, around the inflection point of the basic flow, the negligible values of the buoyancy term, the stabilizing contribution of the viscous dissipation, principally along the walls, and finally the pressure contribution which allows the transfer of energy from the production zones at the center of the layer toward the dissipation zones principally along the walls. When A is increased, the different terms are modified. Note the shift of the shear energy peak toward the upper part of the layer, before the growth of a second peak in the lower part of the layer, the two peaks becoming symmetric in the pure acoustic streaming situation at $A=A_c$. These two peaks are at the limits of the acoustic beam at $|z|\approx 0.15$, and a strong viscous dissipation appears in the same zones. The buoyancy term remains weak and the pressure term, by transfer of energy, allows the local kinetic energy equilibrium. Concerning the perturbations, note first that they evolve from a symmetry with respect to a transverse axis at the center of the layer for $A=0$ toward an antisymmetry with respect to the horizontal midplane for $A=A_c$ so that the perturbations for the intermediate states have no symmetry. The perturbation velocity field corresponds to oblique rolls for $A=0$ and has the shape of an ogive head for $A=A_c$. In the following, we will see the importance of the zones with an oblique flow, where the perturbations u and w are well correlated: these zones are located for $A=0$ at the middle of the layer over a large part of the height, and for $A=A_c$ on both sides of the midplane.

The plots corresponding to the case $H_b=0.8$ are shown in Fig. 17 for $A=50\,000$ (maximum of Gr_c) and $A=A_c=82\,641$ (the results for $A=0$ are those already given for $H_b=0.3$). Note that because of the large values of A, the basic velocities are larger than for $H_b=0.3$. Concerning the contributions to the kinetic energy budget, their evolution is quite similar to that obtained for $H_b=0.3$. The shear energy peaks related to acoustic streaming ($A=A_c$), however, are located closer to the walls and a large zone where the shear energy term is very weak exists at the center of the layer. These modifications are connected to those of the perturbations: the perturbation velocity field of the pure acoustic streaming situation has now almost vertical velocities at the center of the layer and velocities with an oblique direction only exist in two intermediate zones between the central region and the boundary layers.

3. Energetic contributions to the critical Grashof number

To understand the differences between the evolution of the critical curves for $H_b=0.3$ and $H_b=0.8$, we propose another approach based on the expression of the critical Grashof number as a function of energetic contributions. For

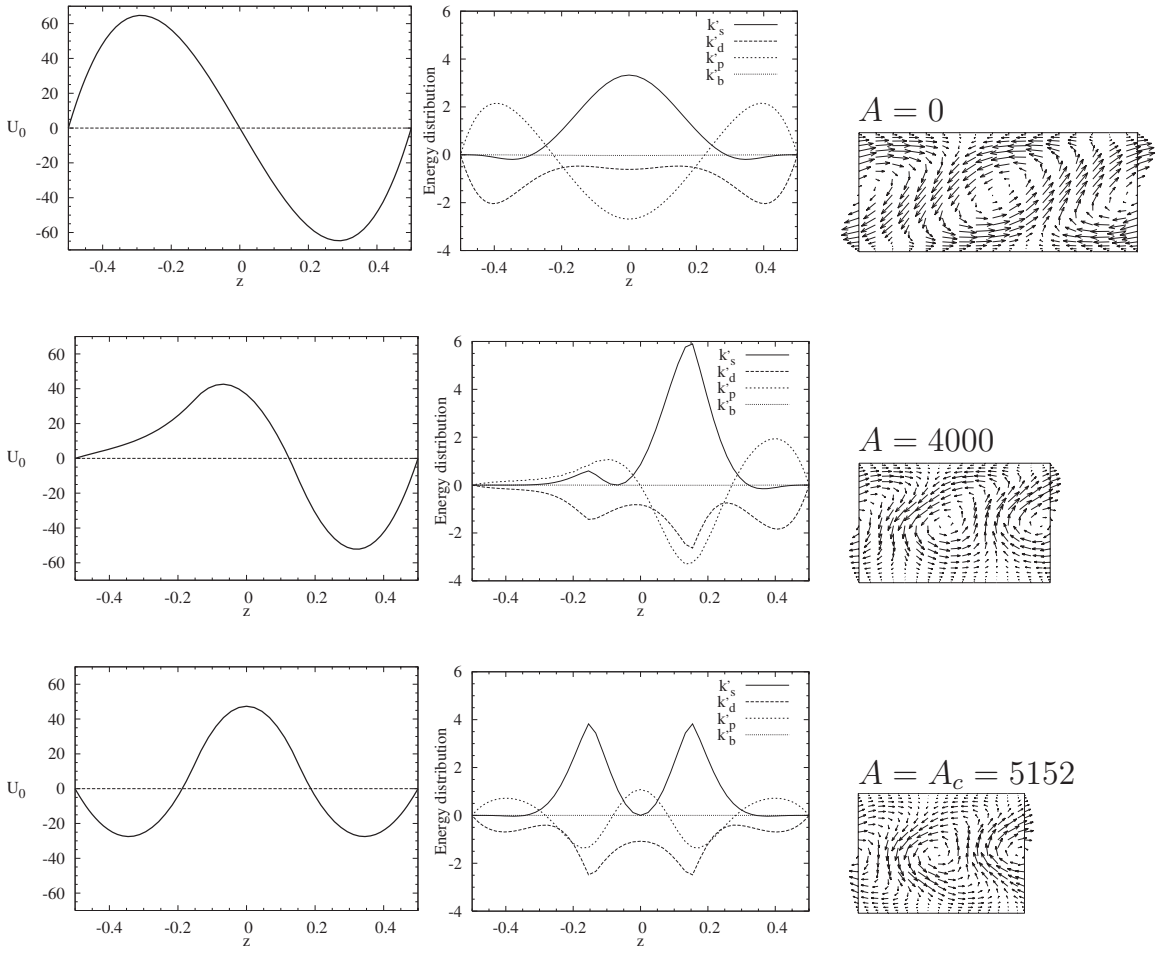

FIG. 16. Spatial structure of the basic flow, the perturbations, and the contributions to the fluctuating kinetic energy budget, for the two-dimensional instabilities at threshold for different values of A. The beam of width $H_b=0.3$ is centered and Pr=0.01. For each value of A, the basic velocity profile $U_0(z)$, the z profiles of the local energy contributions (k_s', k_d', k_b', and k_p'), and the perturbation velocity field in the vertical longitudinal xOz plane are successively plotted.

that, we use the fact that both K'_{s_b} and K'_b linearly depend on Gr. At the threshold, we can write

$$K'_{s_b} = \mathrm{Gr}_c K''_{s_b},$$

$$K'_b = \mathrm{Gr}_c K''_b.$$

From Eq. (18) (with $K'_{d\perp}=0$), we get

$$\mathrm{Gr}_c(K''_{s_b} + K''_b) = 1 - K'_{s_{ac}},$$

which, for $A=0$, i.e., in the pure buoyancy case, gives

$$\mathrm{Gr}_{c_0}(K''_{s_{b_0}} + K''_{b_0}) = 1,$$

where the subscript 0 refers to the case $A=0$. Finally the ratio of these two equations gives

$$\frac{\mathrm{Gr}_c}{\mathrm{Gr}_{c_0}} = \frac{\overbrace{(1 - K'_{s_{ac}})}^{R_{ac}}}{\underbrace{\left(\dfrac{K''_{s_b} + K''_b}{K''_{s_{b_0}} + K''_{b_0}}\right)}_{R_b}}, \tag{23}$$

which indicates that the variation of Gr_c with A can be expressed through the ratio of the two quantities, R_{ac} and R_b, the first quantity being connected to the shear of the basic flow due to acoustic streaming and the second quantity to the shear of the basic flow due to buoyancy (we already saw that the buoyancy energy term remains very weak). For $A=0$, R_{ac} and R_b are equal to 1 and $\mathrm{Gr}_c=\mathrm{Gr}_{c_0}$. These quantities will also eventually decrease, as they tend to 0 for $A=A_c$. The evolution with A of these two quantities R_{ac} and R_b, together with $\mathrm{Gr}_c/\mathrm{Gr}_{c_0}$, are shown in Fig. 18 for $H_b=0.3$ and $H_b=0.8$.

For $H_b=0.3$ [Fig. 18(a)], R_{ac} and R_b continuously decrease from 1 for $A=0$ to 0 for $A=A_c=5152$, but the decrease of R_{ac} is stronger than that of R_b. The values of R_{ac} are then

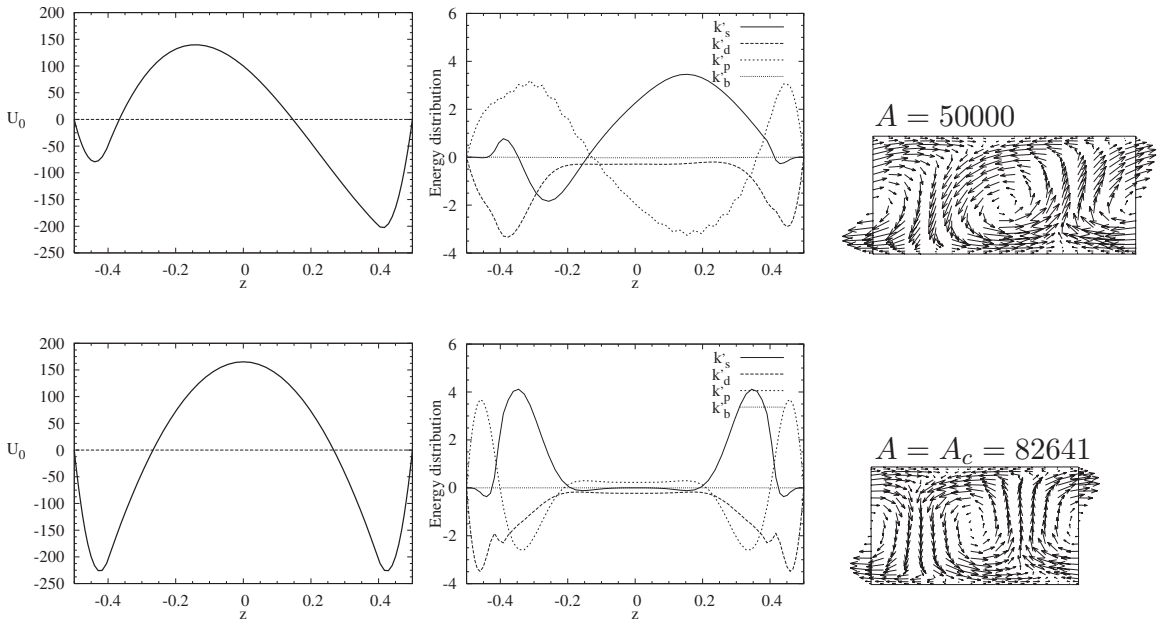

FIG. 17. Spatial structure of the basic flow, the perturbations, and the contributions to the fluctuating kinetic energy budget for the two-dimensional instabilities at threshold for different values of A. The beam of width $H_b=0.8$ is centered and Pr=0.01. For each value of A, the basic velocity profile $U_0(z)$, the z profiles of the local energy contributions (k'_s, k'_d, k'_b, and k'_p), and the perturbation velocity field in the vertical longitudinal xOz plane are successively plotted.

smaller than those of R_b, which explains that Gr_c is always less than Gr_{c_0} and that there is no stabilizing effect in this case. In contrast, for $H_b=0.8$ [Fig. 18(b)], R_b decreases quite strongly with the increase of A whereas R_{ac} because of the slight initial stabilizing effect of the shear term connected to acoustic streaming ($K'_{s_{ac}}<0$ for $A\lessapprox 30\,000$), first slightly increases for $A\leqslant 20\,000$, and then decreases with a progressive increase of the slope. The values of R_{ac} remain larger than those of R_b in a large range of A, which explains the increase of Gr_c beyond Gr_{c_0}, i.e., the stabilizing effect. It is only around $A=78\,000$ that the two curves eventually cross (which corresponds to $\mathrm{Gr}_c=\mathrm{Gr}_{c_0}$), which allows the ultimate decrease of Gr_c toward 0 for $A=A_c=82\,641$. The differences between the cases $H_b=0.3$ and $H_b=0.8$ are better shown in Fig. 19 where the evolutions of R_{ac} and R_b in both cases are plotted as a function of A/A_c. We see that R_b decreases more quickly for $H_b=0.8$ than for $H_b=0.3$, and that, in contrast, R_{ac} has stronger values for $H_b=0.8$ than for $H_b=0.3$.

4. Shear energy analysis at threshold

The variation of the critical thresholds has been shown to depend on the evolution of R_{ac} and R_b which are directly connected to $K'_{s_{ac}}$ and K''_{s_b}, respectively. A detailed analysis of these shear energy terms may then be useful. $K'_{s_{ac}}$ and K''_{s_b} are, respectively, the integrals of the spatial fields $k'_{s_{ac}}$ and k''_{s_b}, which can be decomposed as a product of two terms, one related to the basic flow, $(-\partial U_{ac}/\partial z)$ for $k'_{s_{ac}}$ and $(-\partial U_{b_0}/\partial z)$ for k''_{s_b}, and the other related to the velocity perturbations at the critical threshold Gr_c, $[\mathrm{Re}(wu^*)/|K_d|]$. The z profiles of $(-\partial U_{b_0}/\partial z)$, and those of $(-\partial U_{ac_0}/\partial z)$ for $H_b=0.3$ and $H_b=0.8$ are given in Fig. 20. Note that these profiles are uniquely defined because they do not depend on Gr and A, but to get $(-\partial U_{ac}/\partial z)$ involved in $k'_{s_{ac}}$, we will have to multiply $(-\partial U_{ac_0}/\partial z)$ by A. The z profiles of $[\mathrm{Re}(wu^*)/|K_d|]$, k''_{s_b}, $k''_{s_{ac}}$ and $k'_{s_{ac}}$ for $H_b=0.3$ and $H_b=0.8$ are given in Fig. 21 for increasing values of A from 0 to A_c. For convenience, the profiles for $A=0$ are plotted as thick solid lines and those for $A=A_c$ as thick dashed lines.

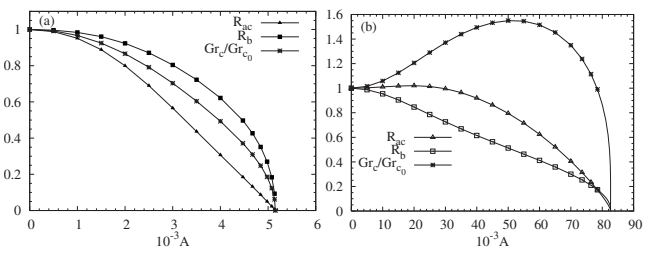

FIG. 18. Evolution of $\mathrm{Gr}_c/\mathrm{Gr}_{c_0}$, R_{ac}, and R_b [see Eq. (23)] for the two-dimensional instabilities as a function of A for (a) $H_b=0.3$ and (b) $H_b=0.8$. The beam is centered and Pr=0.01.

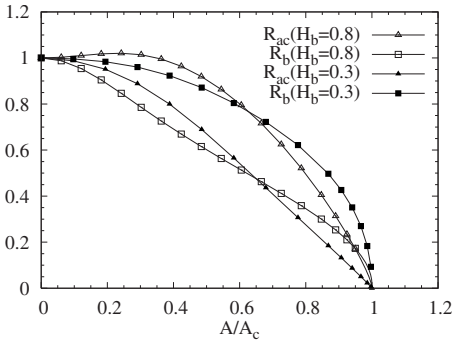

FIG. 19. Evolution of R_{ac} and R_b [see Eq. (23)] for the two-dimensional instabilities as a function of A/A_c for $H_b=0.3$ and $H_b=0.8$. The beam is centered and Pr=0.01.

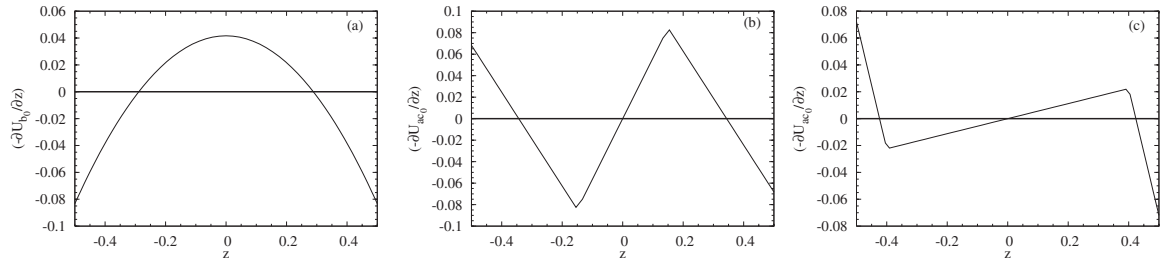

FIG. 20. z-profiles of the basic velocity gradients, (a) $(-\partial U_{b_0}/\partial z)$ (buoyant contribution divided by Gr) and $(-\partial U_{ac_0}/\partial z)$ (acoustic contribution divided by A) for (b) $H_b=0.3$ and (c) $H_b=0.8$. The beam is centered.

Concerning the velocity derivatives (Fig. 20), we first see the different symmetries: symmetry with respect to $z=0$ for $(-\partial U_{b_0}/\partial z)$ and antisymmetry for $(-\partial U_{ac_0}/\partial z)$. $(-\partial U_{b_0}/\partial z)$ [Fig. 20(a)] has positive values at the center of the layer (around the inflection point of the buoyant velocity profile) and negative values close to the boundaries, whereas $(-\partial U_{ac_0}/\partial z)$ [Figs. 20(b) and 20(c)] also change sign from the central part to the boundaries, but because of the antisymmetry, there is also a change of sign between the upper and lower parts of the layer, which imposes a zero value at the center of the layer. If we now compare the profiles of $(-\partial U_{ac_0}/\partial z)$ for $H_b=0.3$ [Fig. 20(b)] and $H_b=0.8$ [Fig. 20(c)] and consider for example the upper part of the layer, we see that the negative values reached at the boundaries are similar in both cases, but that the positive values are very different: for $H_b=0.3$, they are quite strong (slightly stronger than the negative values) with a maximum at the limit of the acoustic beam at $z=0.15$, so quite close to the center of the layer, whereas for $H_b=0.8$, they are weaker (four times less) and the maximum is at $z=0.4$, so rather close to the wall.

We now consider the term related to the perturbations, $[\mathrm{Re}(wu^*)/|K_d|]$, which is plotted in Fig. 21(a). We see that its evolution from the bell-shaped profile at $A=0$ is very different for $H_b=0.3$ and $H_b=0.8$. Note that this profile at $A=0$ is strictly positive (with a maximum close to 0.01) and symmetric with respect to $z=0$, whereas the final profiles at $A=A_c$ are antisymmetric and have mainly positive values in the upper part of the layer and negative values in the lower part. Moreover the profiles at $A=A_c$ for the two values of H_b are very different: for $H_b=0.3$ (still considering the upper part of the layer), we get a positive peak with an intensity of 0.008 around $z=0.15$, so quite close to the center of the layer, and this peak decreases to zero at the center of the layer and at $z=0.4$; for $H_b=0.8$, the peak has a lower intensity (around 0.0026), it is located closer to the wall at $z=0.34$, and its width is quite small so that a zone with almost zero values is found at the middle of the layer for $|z|\leqslant 0.2$. These particular properties of the profiles for $A=0$ and $A=A_c$ explain the variations of $[\mathrm{Re}(wu^*)/|K_d|]$ with A. For $H_b=0.3$, with the increase of A, the buoyant centered peak first increases and moves toward the upper part of the layer (toward the position of the positive acoustic peak). The negative acoustic peak then grows in the lower part of the layer whereas the profile in the upper part decreases in order to eventually fit the positive acoustic peak. For $H_b=0.8$, the evolution is very different: the initial buoyant peak regularly decreases, almost centered at the beginning (with however a slightly quicker decrease in the upper part of the layer) and with a shape which is first flattened and then modulated by the appearance of the two acoustic peaks close to the walls.

The evolution with A of the shear energy profiles due to the basic buoyant flow, k''_{s_b}, looks similar to the evolution of $[\mathrm{Re}(wu^*)/|K_d|]$, and the same differences between the cases $H_b=0.3$ and $H_b=0.8$ are observed [Fig. 21(b)]. Indeed, the large values of $[\mathrm{Re}(wu^*)/|K_d|]$ in the core of the layer are multiplied by the positive values of $(-\partial U_{th_0}/\partial z)$, whereas the weaker values at the boundaries of the layer, which are multiplied by negative values of $(-\partial U_{th_0}/\partial z)$, give negligible contributions. The evolutions with A of k''_{s_b} observed in Fig. 21(b) can be summarized as a quite regular decrease of the buoyant peak for $H_b=0.8$ and as a shift of this peak toward the upper part of the layer with a slight increase, before its decrease combined with the growth of a negative peak for $H_b=0.3$. If we remember that K''_{s_b} is the z integral of k''_{s_b}, these evolutions allow to understand the strong regular decrease of K''_{s_b} (and of $R_b \approx K''_{s_b}/K''_{s_{b_0}}$) for $H_b=0.8$ and the almost constant initial evolution leading to a delayed decrease for $H_b=0.3$. Note that the zero value of K''_{s_b} for $A=A_c$ comes from the antisymmetry of the k''_{s_b} profiles, the zones with negative values counterbalancing the zones with positive values.

The evolution with A of the shear energy profiles due to the basic acoustic streaming flow, $k''_{s_{ac}}$ and $k'_{s_{ac}}$, which are obtained by multiplying $[\mathrm{Re}(wu^*)/|K_d|]$ by $(-\partial U_{ac_0}/\partial z)$ and $(-\partial U_{ac}/\partial z)$, respectively, are shown in Figs. 21(c) and 21(d). Concerning the profiles of $k''_{s_{ac}}$, we see that the values of $(-\partial U_{ac_0}/\partial z)$ near the boundaries are associated with weak values of $[\mathrm{Re}(wu^*)/|K_d|]$ and do not give significative contributions to $k''_{s_{ac}}$. Only the two peaks of $(-\partial U_{ac_0}/\partial z)$ in the core (the positive peak in the upper half of the layer and the negative peak in the lower half) will have an influence. As a result, $k''_{s_{ac}}$ is found to evolve from two peaks with opposite signs (and zero integral) for $A=0$ [i.e., the two peaks of $(-\partial U_{ac_0}/\partial z)$ modulated by the bell-shaped profile of $[\mathrm{Re}(wu^*)/|K_d|]$] toward the two positive peaks of the acoustic streaming shear [correlation between same sign peaks of $[\mathrm{Re}(wu^*)/|K_d|]$ and $(-\partial U_{ac_0}/\partial z)$]. Due to the observed variations of $[\mathrm{Re}(wu^*)/|K_d|]$, the positive peak first increases for $H_b=0.3$, whereas it decreases for $H_b=0.8$ and the negative peak clearly decreases for $H_b=0.3$ whereas it evolves more slowly for $H_b=0.8$. In fact, we are interested by the profiles of $k'_{s_{ac}}$ [Fig. 21(d)] where the linear dependence with A of $(-\partial U_{ac}/\partial z)$ is taken into account. Nevertheless, the evolution

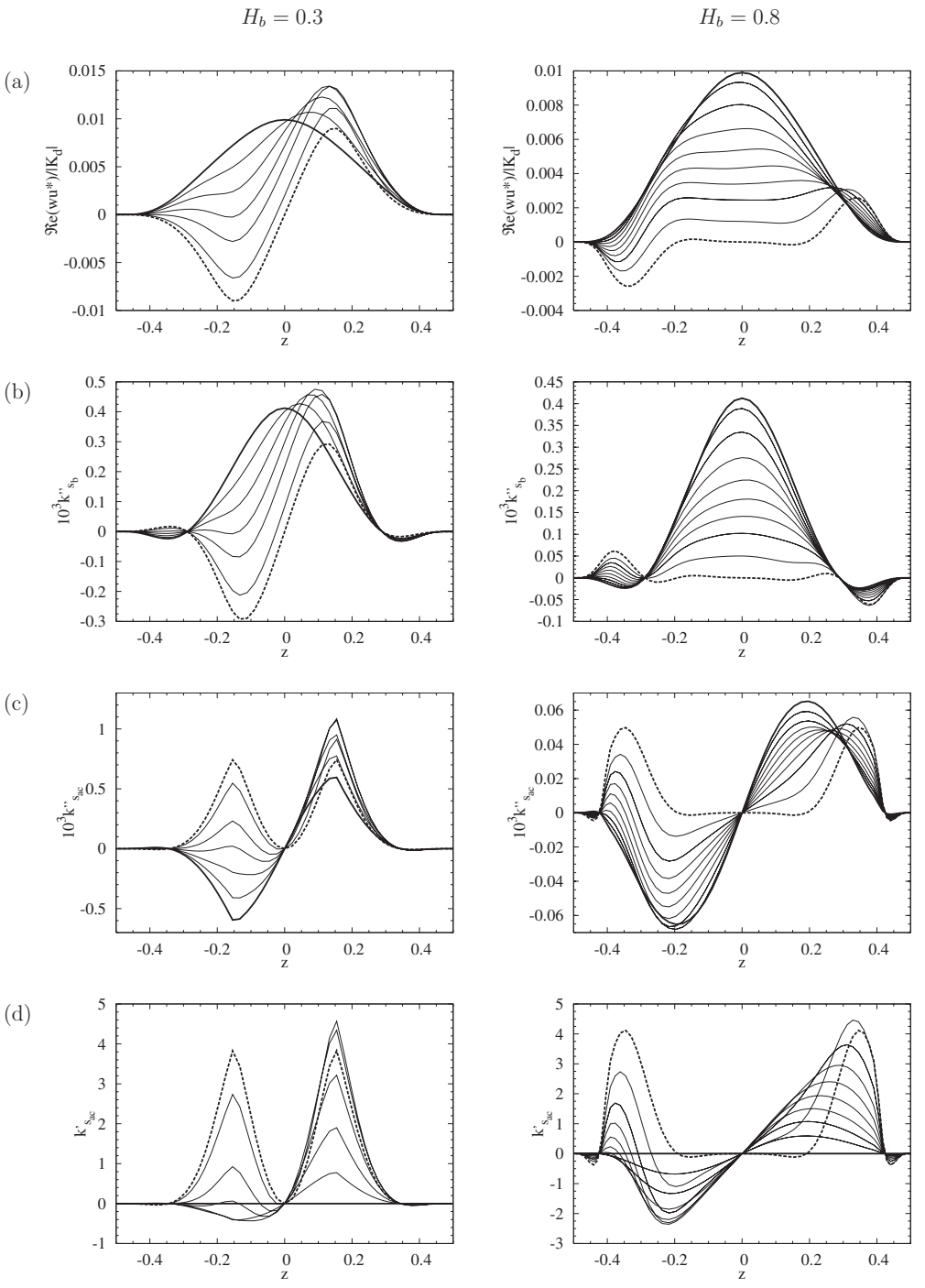

FIG. 21. z profiles of (a) $[\mathrm{Re}(wu^*)/|K_d|]$, (b) k''_{s_b}, (c) $k''_{s_{ac}}$, and (d) $k'_{s_{ac}}$ for the two-dimensional instabilities at threshold for different values of A for $H_b=0.3$ ($A=0$, 1000, 2000, 3000, 4000, 5000, and $A=A_c=5152$) and $H_b=0.8$ ($A=0$, 10 000, 20 000, 30 000, 40 000, 50 000, 60 000, 70 000, 80 000, and $A=A_c=82\,641$). The profiles for $A=0$ are plotted as thick solid lines and those for $A=A_c$ as thick dashed lines. The beam is centered and $\mathrm{Pr}=0.01$. The shear energy terms k''_{s_b}, $k''_{s_{ac}}$, and $k'_{s_{ac}}$ are obtained by multiplying the velocity fluctuation term $[\mathrm{Re}(wu^*)/|K_d|]$ by the basic velocity gradients $(-\partial U_{b_0}/\partial z)$, $(-\partial U_{ac_0}/\partial z)$, and $(-\partial U_{ac}/\partial z)$, respectively.

of $k''_{s_{ac}}$ allows us to understand that for $k'_{s_{ac}}$ (which starts from zero for $A=0$) the increase of A will induce both the initial growth of the negative peak and the growth of the positive peak. For $H_b=0.3$, however, the negative peak will quickly regress and will always be dominated by the positive peak ($K'_{s_{ac}}$ will then be always destabilizing), whereas for $H_b=0.8$, the negative peak is initially stronger than the positive peak which induces an initial stabilizing contribution of $K'_{s_{ac}}$. This explains the slight initial increase of $R_{ac}=1-K'_{s_{ac}}$ for $H_b=0.8$ and the direct decrease for $H_b=0.3$, and, as a consequence, the slower global decrease for $H_b=0.8$ than for $H_b=0.3$.

This analysis has shown the key role played by the evolution of the velocity perturbations (through the term

$[\mathrm{Re}(wu^*)/|K_d|])$ in the evolution of both shear energy terms induced by buoyancy or acoustic streaming, and, through these terms, in the evolution of the critical thresholds for the steady two-dimensional instabilities.

B. Energy budgets for the steady three-dimensional instability

For the three-dimensional instabilities, which have a wave number h_y in the y direction and develop in the transverse yOz plane, it is interesting to distinguish what occurs for the perturbations in the yOz plane and what occurs in the x direction, perpendicular to this plane. Note first that the shear term is in the equation along x because it is the direction of the basic flow, and that the buoyancy term is in the equation along z. Moreover, the pressure is not present in the equation along x because $\partial p/\partial x = ih_x p = 0$. If we consider the local kinetic energy equation, we may distinguish the contributions coming from the velocity equation along x, k'_s, and $k'_{d\perp}$ which equilibrate, and the contributions coming from the velocity equations in the yOz plane, k'_b, k'_p, and $k'_{d\|}$. If we now integrate along z, we have the equilibrium between the shear and viscous contributions coming from the x direction, K'_s and $K'_{d\perp}$, and the equilibrium between the buoyancy and viscous contributions in the yOz plane which may be written as $K'_b = 1$ because the pressure integral is zero and the equations have been normalized by the viscous dissipation in the yOz plane, $|K_{d\|}|$.

The steady three-dimensional instabilities are of Rayleigh-Bénard type and are mainly connected with what occurs in the yOz plane (classical equilibrium between buoyancy and viscous dissipation with a coupling with the temperature perturbation equation), but the flow along x generates a shear term and the corresponding viscous dissipation, in this direction. To better see the couplings between the equations, it is useful to develop the temperature perturbation equation in our case. We get

$$\frac{\partial \theta}{\partial t} = w\frac{\partial T_0}{\partial z} + u\frac{\partial T_0}{\partial x} + \frac{1}{\mathrm{Pr}}\left(-h_y^2\theta + \frac{\partial^2 \theta}{\partial z^2}\right).$$

Note first that the classical Poiseuille-Rayleigh-Bénard situation with a Poiseuille flow along x and a Rayleigh-Bénard instability which develops in the yOz plane is somewhat similar to our case but simpler. In this situation, the basic thermal field depends linearly on z, and we have then $\partial T_0/\partial x = 0$ and $\partial T_0/\partial z = \text{const}$. The temperature perturbation equation is thus only coupled to the velocity perturbations in the yOz plane, and the basic flow velocity U_0 only appears in the velocity perturbation equation along x which is completely decoupled from what occurs in the yOz plane. Then, whatever large is the basic flow velocity, the kinetic energy budget in the yOz plane and the thermal energy budget are unchanged and the critical threshold as well, despite the fact that the total kinetic energy budget is modified because of the growth of the energy components along x in connection with the growth of the basic flow.

In our case, the couplings are different because, on one side, $\partial T_0/\partial z$ depends on the basic flow U_0, which implies that the threshold will also depend on U_0, and, on the other side, $\partial T_0/\partial x$ is different from zero, which implies that the temperature perturbation θ (which is involved in the buoyancy term) is no more independent of the velocity perturbation u along x and that there is a coupling between what occurs in the x direction and what occurs in the yOz plane. In the following, we present the evolution with A of the total and local energy budgets for the steady three-dimensional instability for $H_b = 0.8$.

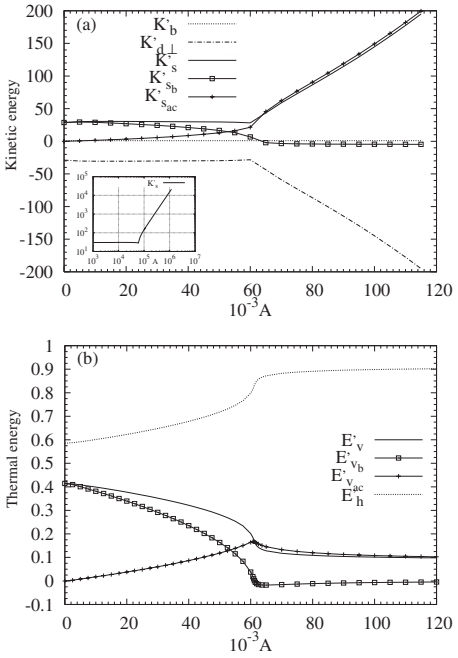

FIG. 22. Variation of the different terms (a) of the total fluctuating kinetic energy budget (K'_b, $K'_{d\perp}$, K'_s, K'_{s_b}, and $K'_{s_{ac}}$) and (b) of the total thermal energy budget (E'_v, E'_{v_b}, $E'_{v_{ac}}$, and E'_h) for the steady three-dimensional instabilities at threshold as a function of the acoustic streaming parameter A for $H_b = 0.8$. The beam is centered and $\mathrm{Pr} = 0.1$. In (a), the evolution of K'_s in log-log scale is given in inset.

1. Total energy budgets

The evolution of the different terms of the kinetic energy budget for the steady three-dimensional instability is shown in Fig. 22(a). We have $K'_b = 1$ which corresponds to the kinetic energy equilibrium in the yOz plane. In the x direction, there is an equilibrium between the shear term K'_s and the viscous dissipation term $K'_{d\perp}$, but these terms have much stronger values. These terms first remain quite constant when A is increased, because the increase of the $K'_{s_{ac}}$ contribution is compensated by the decrease of the K'_{s_b} contribution. A sudden change, however, occurs around $A = 60\,000$, i.e., in the zone of strong decrease of the stability thresholds (Fig. 12). Beyond this value of A, we approach an asymptotic behavior: the term K'_{s_b} quickly reaches a negative constant value, which indicates a stabilizing contribution (this contribution is weak with respect to the other terms), whereas the terms K'_s, $K'_{s_{ac}}$, and $|K'_{d\perp}|$ strongly increase and reach a A^2 law [this law is highlighted in the inset in Fig. 22(a) where the evolution of K'_s is plotted in a log-log scale]. The thermal energy budget given in Fig. 22(b) shows that both thermal

energy transport terms, E'_v and E'_h, are destabilizing terms, but E'_h is the dominant term. A change is also observed around $A=60\,000$: before this value, we see an increase of E'_h and a decrease of E'_v, whereas beyond this value both terms quickly tend towards an asymptotic value which is 0.9 for E'_h and 0.1 for E'_v. Finally, the decomposition of E'_v into its two contributions allows to see how this term evolves from initial values mainly determined by E'_{v_b} to final values mainly determined by $E'_{v_{ac}}$.

The transition around $A=60\,000$ is associated with the fact that the basic velocity profiles change very quickly at this value, from profiles dominated by Gr to profiles dominated by A. This occurs because, for the initial values of A, the values of Gr_c are strong, which masks the acoustic streaming contributions, whereas, around $A=60\,000$, the very strong decrease of Gr_c allows the acoustic streaming contributions to become suddenly dominant. Beyond this value of A, $(-\partial U_0/\partial z)$ and $(\partial T_0/\partial z)$ vary proportionally to A, whereas $(\partial T_0/\partial x)$ is still constant. Asymptotic behaviors are also found for the different perturbations, $|v|/|w| \sim \mathcal{O}(1)$ and $|u|/|w| \sim |\theta|/|w| \sim \mathcal{O}(A)$, and also for the threshold, $\mathrm{Gr}_c \sim 1/A$, whereas the characteristic dimensions y and z become constants. As a consequence, the normalized kinetic energy contributions in the yOz plane vary as $\mathcal{O}(1)$, and those in the x direction vary as $\mathcal{O}(A^2)$ [the negligible K'_{s_b} contribution vary as $\mathcal{O}(1)$]. These asymptotic variations perfectly agree with the evolutions observed in the kinetic energy budgets presented in Fig. 22(a). Concerning the thermal energy contributions, if they were normalized by $|K_{d\|}|$ as for the kinetic energy budgets, they would vary as $\mathcal{O}(A^2)$, except the negligible vertical transport of temperature due to buoyancy which would vary as $\mathcal{O}(1)$. These variations, however, are not visible in Fig. 22(b) because the contributions have been normalized by one of the terms of the budget, the dissipation term by conduction.

2. Local energy budgets

The local energy budgets for the steady three-dimensional instability are shown in Fig. 23 for four values of A, $A=0$, 20 000, 60 000, and 100 000. We also give the z profiles of the basic velocity U_0 and temperature T_i and the perturbation velocity field in the vertical transverse yOz plane. For $A=0$ [Fig. 23(a)], we see that, in the yOz plane, the buoyancy term k'_b is destabilizing in two zones close to the walls where the basic temperature field is inversely stratified, which confirms that the instability is of Rayleigh-Bénard type. But the situation is more complex than the usual Rayleigh-Bénard situation because the temperature perturbation θ is not only connected to the vertical transport of the temperature but is also connected to the horizontal transport of the temperature through the constant temperature gradient $(\partial T_0/\partial x)$ and the u velocity perturbation in the x direction. In this x direction, the kinetic energy contributions are very strong: we mainly find two destabilizing shear peaks near the walls balanced by stabilizing viscous dissipation peaks. The thermal energy budget also gives destabilizing peaks of e'_v and e'_h near the walls. Finally, the perturbation velocity field shows that the instability takes the form of counter-rotating rolls of Rayleigh-Bénard type which develop in each of the two zones with inverse stratification near the walls. The rolls have the same direction of rotation in the upper and lower zones, and the descending velocities $(w<0)$ in the center are associated to negative temperature perturbations θ in order to get a destabilizing buoyancy term. Finally, note that the rotating motion inside the rolls is modulated by the longitudinal velocity perturbation u, the descending velocities in the yOz plane $(w<0)$ being mainly correlated with positive longitudinal velocities $(u>0)$.

When A becomes different from zero [Figs. 23(b)–23(d)], the two inverse stratification zones are no more symmetric and the instability only develops in the lower zone which becomes dominant (the development of the instability in the upper zone would need a larger value of Gr_c). For moderate values of A, the energy contributions and the perturbations look similar to those obtained for $A=0$, but they only exist in the lower half of the layer, and, in particular, counter-rotating rolls are only obtained near the bottom wall. Note that, compared to the case $A=0$, the intensity of the energy peaks has doubled. In fact, these terms are normalized with respect to the total dissipation terms ($|K_{d\|}|$ for the kinetic energy and $|E_d|$ for the thermal energy) which have been reduced by half because they now only integrate contributions in the lower part of the layer. When A is increased, the perturbation zone at the bottom of the layer extends in connection with the extension of the inverse stratification zone at the bottom, which favors the onset of instability in this zone despite the slower stratification effect (note that the effective Gr depends on the cube of the effective height, but its dependence on the effective ΔT is only linear) and leads to a decrease of Gr_c. When A is increased beyond the transition value around $A=60\,000$, the basic profiles become dominated by acoustic streaming, and the temperature field, in particular, is inversely stratified on the whole lower half of the layer [Fig. 23(d)]. For larger A, the extent of this zone with inverse stratification does not change, but the intensity of the stratification linearly increases with A ($T_b \ll T_{ac}$ and T_{ac} proportional to A), which induces the decrease of Gr_c as $1/A$. In this asymptotic domain [Fig. 23(d) for $A=100\,000$], even though the inverse stratification is limited to the lower half of the layer, we see that the perturbations and, in particular, the counter-rotating rolls extend on almost the whole height of the layer. Moreover, we have seen that the u velocity scales as $\mathcal{O}(A)$ compared to the velocity components involved in the rolls, v and w. As a result, the rotating motion along the roll is strongly modulated by the u velocity perturbation, which generates three-dimensional trajectories with large variations in the x direction. Finally, as we know that the wavelength of the perturbation corresponds to the horizontal space occupied by two counter-rotating rolls and that, in the Rayleigh-Bénard situation, the rolls are almost circular, the observed increase of the wavelength with A may be explained by the increase of the size of the rolls which only occupy four tenths of the height for $A=0$ but occupy almost the whole height for $A=100\,000$.

Although we mainly based our analysis on the inverse vertical stratification of temperature, we recall that this instability is not purely of Rayleigh-Bénard type and that in the thermal energy budget, beside the classical vertical transport

of temperature, is also involved, even in a large manner (90% of the thermal energy production in the asymptotic domain), the horizontal transport of temperature connected to the horizontal temperature gradient ($\partial T_0/\partial x$) and to the strong perturbation velocity u.

VII. CONCLUDING REMARKS

Our linear stability analysis of the flows induced in a fluid layer by buoyant convection and acoustic streaming has given interesting information on the instabilities which develop in such flows and on the way they are modified when acoustic streaming is enhanced.

First, pure acoustic streaming flows are sensitive to a shear instability which develops as a right traveling wave in the plane of the flow (two-dimensional instability) and is due to the strong shears present in these flows at the limits of the ultrasound beam. The thresholds A_c (critical value of the acoustic streaming parameter) for this oscillatory instability depend on the normalized width H_b of the ultrasound beam, with a minimum for H_b=0.32. If the ultrasound beam of fixed width is decentered, the thresholds first decrease and then increase when the beam gets closer to one of the walls. This change of variation is associated with a transition from right to left traveling waves.

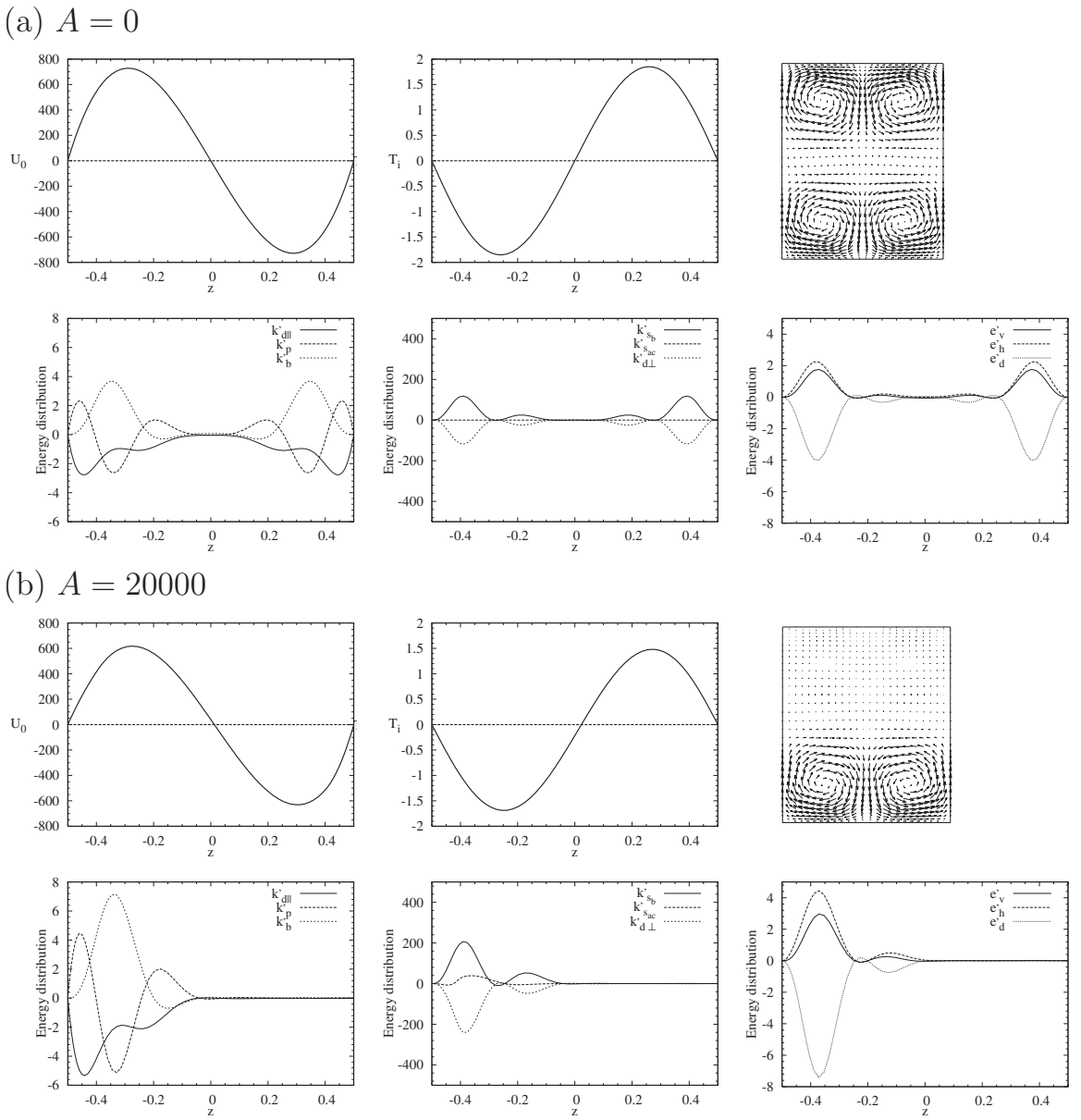

FIG. 23. Spatial structure of the basic flow, the perturbations, and the contributions to the fluctuating energy budgets for the steady three-dimensional instabilities at threshold for different values of A. The beam of width H_b=0.8 is centered and Pr=0.1. For each value of A, the basic velocity profile $U_0(z)$ and thermal profile $T_i(z)$, the perturbation velocity field in the vertical transverse yOz plane, and the z profiles of the local fluctuating contributions to the kinetic energy budget in the yOz plane ($k'_{d\|}$, k'_p, and k'_b) and in the x direction (k'_{s_b}, $k'_{s_{ac}}$, and $k'_{d\perp}$) and to the thermal energy budget (e'_v, e'_h, and e'_d) are successively plotted.

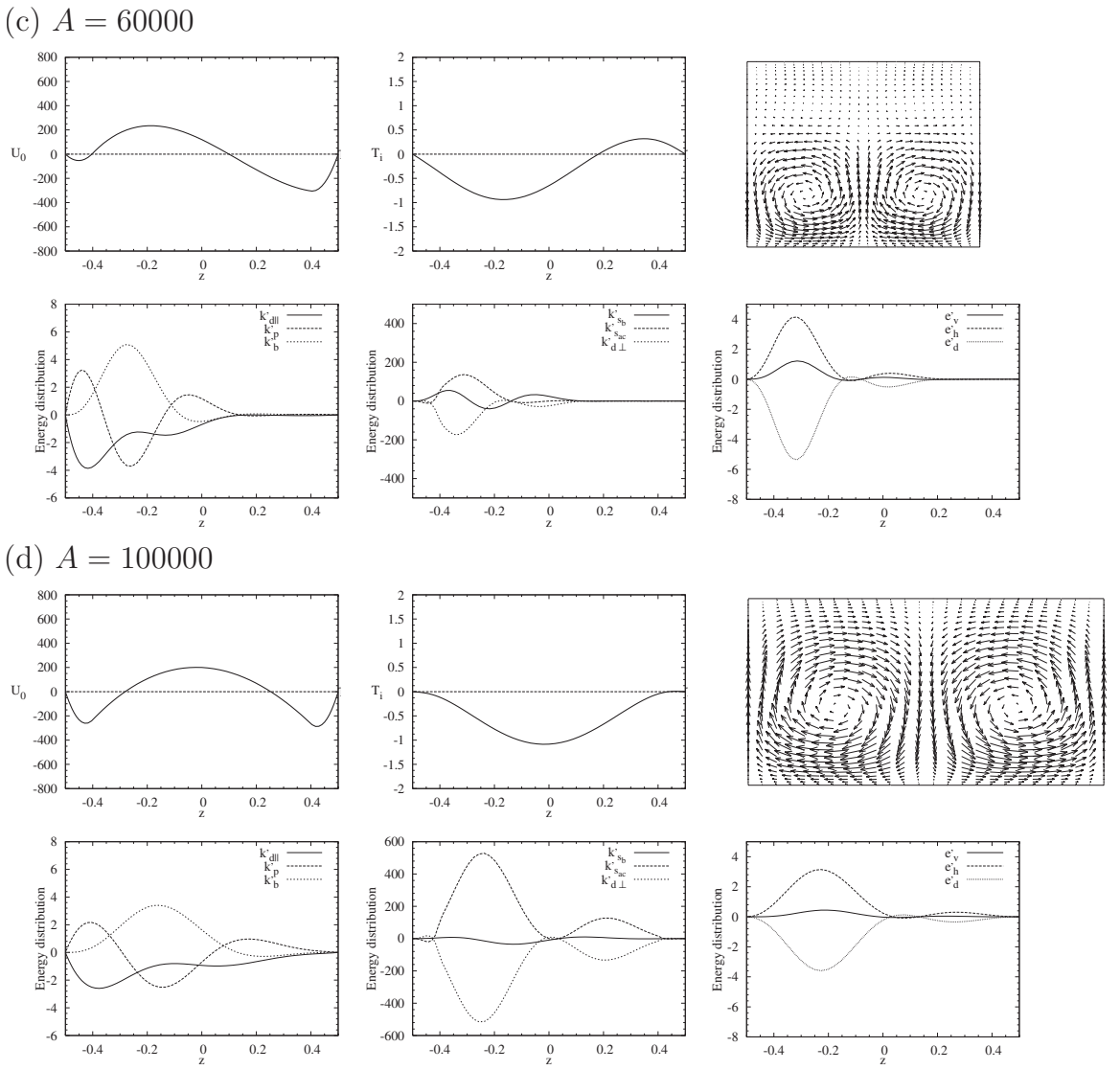

FIG. 23. (*Continued*).

Acoustic streaming also affects the stability of the buoyant convection. The two-dimensional steady shear instability, which is dominant for the small values of the Prandtl number Pr, becomes oscillatory when acoustic streaming is applied. Depending on the width of the beam, the thresholds Gr_c (critical value of the Grashof number) will first decrease with the increase of the acoustic streaming parameter A (small widths) or increase (large widths). A stabilizing effect is then obtained for large width beams, but, for any width, the thresholds will eventually decrease and reach $\mathrm{Gr}=0$ at the value of A_c obtained for a pure acoustic streaming flow. The three-dimensional oscillatory instability, which prevails for intermediate values of Pr, is regularly stabilized when acoustic streaming is applied. Finally, the three-dimensional steady instability of Rayleigh-Bénard type, which occurs at large Pr, is strongly destabilized when the acoustic streaming parameter A is enhanced, with thresholds eventually decreasing asymptotically to zero with a $1/A$ law. The decentring of the beam is another way to modify the thresholds: it is found that a stabilizing influence can be obtained when the beam is decentered in such a way that the streaming induced by the beam opposes the buoyant flow.

In order to understand the stabilizing or destabilizing mechanisms involved when acoustic streaming is applied, an analysis of the fluctuating energy budget associated with the disturbances at threshold was performed. The modifications affecting the two-dimensional shear instability thresholds are strongly connected to modifications of the velocity fluctuations which enter the destabilizing shear energy term as a product. This velocity fluctuation product evolves, when acoustic streaming is applied, from a peak contribution at the center of the layer (buoyant flow) to two peak contributions at the limits of the ultrasound beam (acoustic streaming flow). Depending on the beam width, the two "acoustic streaming" peaks will be close one to the other (small widths) or separated by a no-fluctuation zone (large widths), and that will induce strongly different evolutions of the velocity fluctuation product with the increase of the acoustic streaming parameter. Such different evolutions are a key factor to explain the either destabilizing (small widths) or sta-

bilizing (large widths) effect induced by acoustic streaming on the two-dimensional shear instability. Concerning the three-dimensional steady instability of Rayleigh-Bénard type, the spectacular decrease of the thresholds induced by acoustic streaming is explained by the extension of the zone with inverse thermal stratification at the bottom of the layer. When the influence of Gr_c (after its strong decrease) is dominated by that of the acoustic streaming parameter A, the basic profiles become close to acoustic streaming profiles, with, in particular, a zone with inverse stratification extending over the whole lower half of the layer. Further increase of A will not change the size of this zone, but will amplify the stratification proportionally to A, which explains the asymptotic variation of the thresholds Gr_c as $1/A$.

These results clearly show that no systematic stabilizing effect of the buoyant convection is obtained by applying acoustic streaming. Stabilizing effects may, however, be obtained through an adequate choice of the beam width, beam position, and acoustic intensity. And destabilizing effects can also be promoted for applications which would need more fluctuating flows. All this indicates that acoustic streaming has to be used with care.

[1] G. Müller and A. Ostrogorsky, in *Handbook of Crystal Growth: Growth Mechanisms and Dynamics*, edited by D. T. J. Hurle (North-Holland, Amsterdam, 1993), Vol. 2b.

[2] A. Müller and M. Wiehelm, Z. Naturforsch. A **19**, 254 (1964).

[3] M. Faraday, Philos. Trans. R. Soc. London **121**, 229 (1831).

[4] J. Lighthill, J. Sound Vib. **61**, 391 (1978).

[5] W. L. Nyborg, *Nonlinear Acoustics*, edited by M. F. Hamilton and D. T. Blackstock (Academic Press, San Diego, 1998), p. 207.

[6] C. Eckart, Phys. Rev. **73**, 68 (1948).

[7] Lord Rayleigh, *The Theory of Sound* (MacMillan, London, 1929).

[8] O. V. Rudenko and A. A. Sukhorukov, Acoust. Phys. **44**, 565 (1998).

[9] K. D. Frampton, S. E. Martin, and K. Minor, Appl. Acoust. **64**, 681 (2003).

[10] C. Suri, K. Takenaka, H. Yanagida, Y. Kojima, and K. Koyama, Ultrasonics **40**, 393 (2002).

[11] G. N. Kozhemyakin, V. G. Kosushkin, and S. Y. Kurochkin, J. Cryst. Growth **121**, 240 (1992).

[12] G. N. Kozhemyakin, J. Cryst. Growth **147**, 200 (1995).

[13] G. N. Kozhemyakin, J. Cryst. Growth **149**, 266 (1995).

[14] G. N. Kozhemyakin, J. Cryst. Growth **257**, 237 (2003).

[15] W. Dridi, D. Henry, and H. Ben Hadid, Phys. Rev. E **77**, 046311 (2008).

[16] G. N. Kozhemyakin, L. V. Zolkina, and M. A. Rom, Solid-State Electron. **51**, 820 (2007).

[17] H. Lei, D. Henry, and H. Ben Hadid, Int. J. Heat Mass Transfer **49**, 3601 (2006).

[18] W. Dridi, D. Henry, and H. Ben Hadid, J. Cryst. Growth **310**, 1546 (2008).

[19] W. Dridi, D. Henry, and H. Ben Hadid, C. R. Mec. **335**, 175 (2007).

[20] W. Dridi, D. Henry, and H. Ben Hadid, C. R. Mec. **337**, 238 (2009).

[21] M. G. Braunsfurth, A. C. Skeldon, A. Juel, T. Mullin, and D. S. Riley, J. Fluid Mech. **342**, 295 (1997).

[22] S. Kaddeche, D. Henry, and H. Ben Hadid, J. Fluid Mech. **480**, 185 (2003).

[23] P. Laure and B. Roux, C. R. Acad. Sci. Paris **305**, 1137 (1987).